Summer 2018

An investigation of measurement method and phase change in a latent heat energy storage device

Jared Becker
University of Iowa

AN INVESTIGATION OF MEASUREMENT METHOD AND PHASE CHANGE IN A LATENT HEAT ENERGY STORAGE DEVICE

By

Jared Becker

A thesis submitted in partial fulfillment

of the requirements for the Master of

Science degree in Mechanical Engineering

in the Graduate College of

The University of Iowa

August 2018

Thesis Supervisor: Professor H.S. Udaykumar

Graduate College
The University of Iowa
Iowa City, Iowa

CERTIFICATE OF APPROVAL

_____

MASTER'S THESIS

_____

This is to certify that the Master's thesis of

Jared Michael Becker

has been approved by the Examining Committee for the thesis requirement for the Master of Science degree in Mechanical Engineering at the August 2018 graduation.

Thesis Committee: _____
H.S. Udaykumar, Thesis Supervisor

_____
James Buchholz

_____
Hongtao Ding

...

To my Family and Friends

...

AKNOWLEDGMENTS:

First and foremost, I would like to thank Professor Uday Kumar for providing me the opportunity of working on this project. With his mentorship, charisma and patience I found greater depth in myself as well as a path to experience the beauty, wonder and expanse that is scientific knowledge. I am very grateful to have been able to learn from him. I would also like to thank Professor James Buchholz for offering me depth and perspective in many of my most challenging hours. I consider myself lucky to be among those who have experienced his passion and mentorship. I would also like to thank Professor Hong Tao Ding for sitting on my committee. I am grateful to have been able to learn under all of your guidance.

I would also like to thank my lab mates: Nirmal, Oishek, Mike, Sid, Pratik, Alexia, Moustaffa, Ehsan, Kayley, Aaron, and Sangyup; in addition to, honorary lab mates: Jake, Srivats and Sarah, for the countless hours spent meandering life's vicissitudes. My time with you all, without doubt, comprises my most memorable graduate school experiences.

To my classmates: Dillon Hefel, Anna English, and Danielle Culver, I want express my gratitude for aiding me in the onset of this project. Your fortitude and alacrity brought joy into our countless sleepless nights.

To Liana Suleiman, I want to thank you for the countless hours you took out of your schedule to aid me in the lab. You brought key strategies to several of the tests run in this project.

To Tori, I would like to express my love and gratitude for your support and sacrifice. Your patience and motivation was often what I needed when the straights seemed narrow and dire.

To my Dad, Mitchell Becker, and the rest of my family, I owe you the world. Your support would consistently supplanted my stress with focus and positivity. Thank you for always being with me.

ABSTRACT:

Recent work in sustainable energy science explores solar cooking technologies as a means to ameliorate issues tied to solid fuel dependence. Exploring uses of two-phase mixtures as a way to store peak solar energy for off-peak usage is a novel approach that has been gaining attention in recent years. This research explores a "solar salt" mixture (40%wt KNO_3 and 60%wt $NaNO_3$) in an aluminum enclosure under two test conditions: conduction enhancement and no conduction enhancement. The central aim is to develop an understanding of thermal distributions and melt developments as the system moves from room temperature to 300 ^oC. Thermal pattern development is explored by experimentally observing a 2-D temperature field at 8 co-planar points, comprised of 3 radial positions with complementary circumferential measurements, using thermocouples. The instrument array is traversed to three different axial positions where collected data is compared with results from a numerical solver. Results find three important details. First, the melt pattern of the fin experiments show quicker rates of melting after the onset of melt at the bottom of the enclosure. Second, the spatial effects of the instrumentation influence the presence of thermal phenomena. Lastly, approximations of the salts behavior using numerical simulations are supported in identifying phases of melt development.

PUBLIC ABSTRACT:

Solid fuel dependence in the developing world is a pervasive issue with far-reaching implications. Recent trends in humanitarian organizations explore sustainable cooking technologies as a means to ameliorate issues tied to solid fuel dependence. A solution of growing interest in the scientific community is the storage of peak solar energy for later cooking use; particularly, by using latent heat storage materials.

In addition to creating a dataset useful for computational simulation and investigating an experimental measurement method, this work is designed to evaluate the charging and discharging of a thermal energy storage material. The primarily purpose is to shed light on the behavior of a solar salt mixture undergoing phase change. The key results from this project show vertical internal fins aid the system in rapid energy charge and discharge. Second, the measurement method highlights its presence can influence the development thermal physics . Third, the numerical solver modeled experiments closely and was significant to understanding the development of melt patterns.

TABLE OF CONTENTS

LIST OF TABLES

LIST OF FIGURES

Chapter I – Introduction

This work contributes to global sustainability measures by investigating technology capable of supplanting unclean domestic cooking fuels with clean energy technology. A term describing such initiatives is 'leap-frogging technology; or more formally, methods which guide developing countries into modernization without following environmentally destructive industrial growth models implemented by wealthier nations [1].

1.1 Motivation

In 2004, solid fuels were estimated to cause 1.6 million excess deaths annually and over 38.5 million disability-adjusted life years (DALYs) [2]. In 2012, a study conducted by the World Health Organization (WHO) found that figure to have grown from 1.6 million to 4.3 million annual deaths—a mortality rate twice as great as malaria and AIDS/HIV combined [3,4,5]. This makes indoor air pollution (IAP) the most important environmental cause of disease, after contaminated water and lack of sanitation [6,7,8]. Health implications have secondary economic effects too: one 2003 study found that over $50 billion is spent annually directly on medical costs used to treat the effects of indoor air pollution (IAP), and that was fourteen years ago [9]. However, studies compounding medical costs in conjunction with the fuel energy envelope found a $34 billion investment could generate $104 billion worth of economic benefits[10,11]. Another resulting side effect is environmental degradation and lost economic opportunity.

Firewood and charcoal, used for domestic energy consumption, represents approximately 55% of the global wood harvest, in which, 27-34% is harvested in a manner that surpasses

the arboreal regrowth rate [12,13] . Depleting surrounding fuel sources requires these individuals to travel greater distances to collect fuel[14]. The time lost to illness and gathering wood fuel weakens the opportunities for these individuals to pursue higher forms of economic viability.

Leapfrogging technology is one solution—it has reducing effects on climate change and many metrics show correlations of enhanced social and economic outcomes from incorporating clean energy consumption and air quality into people's daily lives [15]. Failure to address these issues has long-term, and likely irreversible, global health, environmental and economic consequences[16,17,18]. Luckily, modern sustainable energy technologies are developing in tandem with the developing world's increased energy throughput. Addressing the damages caused by solid fuel dependence is complex; it requires the successful development and implementation of a practical solution that can overcome multi-faceted challenges. Our group suggests the investigation of solar cooking technology.

Most territories in low- and middle- income countries exist as an amalgamation of several independent cultures, languages and traditions; to address this, the scientific community has been considering more "holistic" or "end-use" approaches for solar cooker design as opposed to the traditional solar cooking methods that require the user to cook outdoors during the daytime. As a result, energy scientists have invested in the development of cookers that are capable of discharging heat during the evenings and mornings, allowing users to cook when the sun is not available. Such measures allow the possibility for individuals to cook indoors, at any hour and in any location inside the home—a range of cooking flexibility that

traditional methods do not offer. Although a small step, enhancing solar cooking methods allows for a more convenient and private cooking experience.

One of the most common methods of storing peak solar energy for off peak usage is the utilization of energy storage systems, in particular latent heat energy storage (LHES) materials. LHES material properties offer a high energy storage to volume ratio, making them ideal candidates for energy storage cook stoves. However, implementing a LHES device for commercial use requires one to overcome several challenges inherent to the energy storage, primarily the charge and discharge rate.

LHES materials appropriate for solar cooking are notoriously known for having poor thermal conductivities. Their inherent inability to rapidly discharge and charge impedes its functionality. Researchers have investigated several novel approaches to ameliorate this issue such as introducing high conductivity porous materials, nano particles, metal matrices and extended surfaces among others as conduction enhancement methods [19–23]. Among these methods, extended surfaces are the most popular choice as they are a simple and low-cost strategy for controlling the temperature gradient and lift within a given system [23–25].

The efficacy of using extended surfaces, or fins, over other conduction enhancement methods is twofold. First, high conductivity fins attached to a central core allows for the system to handle the asymmetries of the heat input regarding charging and discharging, secondly, the manufacturing, maintenance and augmentation of finned conduction enhancement offers greater simplicity and cost effectiveness when compared to the other methods.

Significant work has been done showing the increases thermal transport properties as a function of finned conduction enhancement, however most studies fail to address the fact that latent heat energy storage device effectiveness is not only dependent on the conductivity but also the fluid viscosity, aspect ratio, container size, length, volume, and fin arrangement. The complexity of the design space makes understanding how resulting convective flow patterns and melt front developments effect the overall efficiency of the thermal cycle. Given the numerous parameters, a parametric study is experimentally impractical. What formally needs to be understood is the physics that govern phase change in a latent heat energy storage device, which later, could lend to deeper and wider investigations. What this work begins to show is that the effectiveness of a given design is directly proportional to convective cell growth in the early stages of energy input.

Little work has been done to characterize spatial temporal patterns in the transition regions as the thermal energy storage device moves between solid and liquid states primarily because high temperature solar salt experiments offer numerous challenges: the materials are often opaque, and require special containerization. Therefore, this project is designed to better understand these physics and generate data that characterizes the thermal phenomena that govern phase change in a thermal energy storage device.

Chapter II – Background

This chapter discusses why thermal energy storage materials are important to modern day energy systems, and offers a brief account of their history and function.

2.1 Solar Thermal Energy Storage

The utilization of thermal energy storage (TES) systems begins with the need to meet global environmental impacts of domestic and industrial energy consumption. New and innovative ways of applying energy storage technology has been a subject of study among scientists for the last half century. As a result, utilizing TES systems to store peak solar energy for domestic cooking applications has garnered great attention in last decade. One application of this renewed interest in thermal energy storage is the possibility of offering health, environmental and economic relief due to solid fuel dependence. The investigation of a material suitable for such a device is the subject of this study. Examining two modes of TES—sensible and latent—provides the groundwork for the experimental design.

2.1.1 Sensible Heat

Sensible heat storage—heat that can be readily gauged by human senses—refers to energy stored by changing the temperature of a given material. The amount of energy stored is a function of the heat capacity and storage mass. In short, sensible heat systems transfer energy across its system boundary while remaining in a single state. Some examples of sensible heat systems are propylene glycol geothermal loops, or packed rock beds for cooking or space

heating [26]. Assuming steady state conditions, sensible heat storage can be readily calculated using equation 1.

$$Q = \int_{T1}^{T2} mc_p dT \quad (1)$$

Q = energy storage
$T1$ = initial temperature
$T2$ = final temperature
m = mass of the storage system
c_p = specific heat at constant pressure

Despite the prevalence of sensible heat energy systems they are the least effective method of storing thermal energy. The amount of energy that can be stored per unit volume is limited by the state of the material. Additionally, regulating the discharge temperature of a single phase material is generally impractical. Therefore, solar thermal industries have steered towards using latent heat materials as opposed to purely sensible heat materials.

2.1.2 Latent Heat

Latent heat energy storage (LHES) materials are well documented with their earliest roots tracing back to cold food preservation. Despite several commercial innovations throughout the early 1900s, it wasn't until Dr. Maria Telkes's first practical application of sodium sulfate decahydrate (Na_2SO_4 $10H_2O$), better known as "Glauber's salt", in solar ovens [27] and the "dover house experiment" [28, 29] in 1946, did LHES research find a solid foundation among the scientific community [28]. Her contributions to the field are widely regarded for expanding the reach of LHES systems from being a primitive technology to a choice thermal material. As a result, LHES material science has evolved to consider the potential of several crystalline chemical compounds and mixtures with wide ranging applications in commercial and industrial processes [30,31,32].

Latent heat energy storage (LHES) systems function by utilizing energy inputs to illicit a reversible phase change. At the transition temperature, the solution experiences a near isothermal state change until the mass has moved beyond its transition temperature. The energy required for this phenomenon to take place is known as the latent heat of fusion. It is common that a material exhibits two types of phase change during heating and cooling: a solid – solid (S-S) and solid-liquid (S-L) phase change. In most cases the S-L transformation stores more thermal energy per unit mass then the S-S phase change and is the region engineers target when designing LHES devices. Assuming steady state conditions, the energy content of a latent heat storage material can be calculated using equation 2.

$$Q = \int_{T1}^{Tm} mc_{ps}dT + \int_{Tm}^{T2} mc_{pl}dT + f_m m\Delta h_m \quad (2)$$

T_m = melt temperature
Δh_m = latent heat of fusion per unit mass
f_m = melted fraction of material
C_{ps}= avg specific heat of the solid state
c_{pl} = avg specific heat of the liquid state

As seen, LHES materials energy storage capacity is comprised of two sensible heat terms. Typically, it is advantageous to design a system to be dominated by the latent heat term, however, utilizing the sensible heat terms maximizes the energy storage potential of a system.

TES materials can be divided into three main categories, as shown in Figure 1 [33] . The number of compounds and mixtures that fall within these categories to date is innumerable; therefore, selecting the most apposite material for a given energy problem is one of several major engineering challenges. However, the general requirements for this project makes it possible to reject a majority of materials before a detailed analysis takes place.

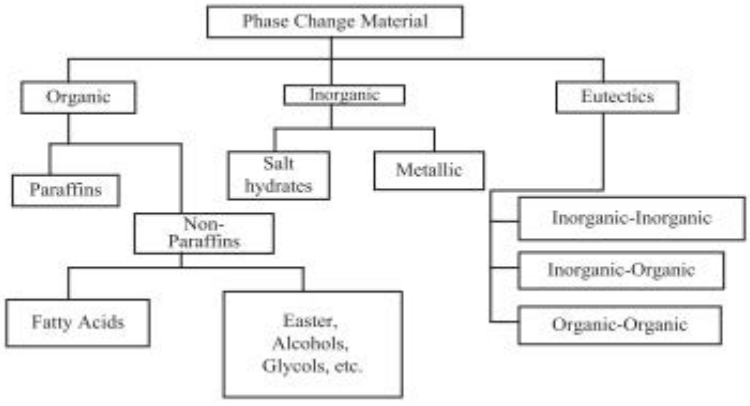

Figure 1: Classifications of PCMs [33]

Organics comprised of Paraffin and paraffin waxes exist as part of a family of saturated hydrocarbons; as opposed to non-paraffins, which are comprised of a different esters, fatty acids, alcohols, and glycols [33]. Both are widely available and exhibit great chemical stability. However, their disadvantages of low melting points, price, and high liquid volume expansions rules them out from being a choice energy storage material for solar cooking.

Metallic phase change materials include low melting temperature metals and metal eutectics; however, most commercial applications won't consider metallic materials due to their weight, and cost. This leaves inorganics.

Inorganics offer higher melting points and energy storage densities at a significantly reduced cost all while featuring good chemical stability. Inorganics can be organized into 3 categories: anhydrous salts, salt hydrates and metallics. Salt hydrates are the oldest and most studied phase change materials and exhibit high thermal diffusion properties relative to the other inorganic materials. The liquid content of the hydrated medium is the main contributing factor to its relatively high thermal conductivity, however, their liquid content also creates a strong tendency towards phase segregation. This decreases the TES device's effectiveness and reliability. A preventative measure typically taken to combat phase segregation is to hermetically seal the enclosure under pressure, so the operating conditions do not exceed the vaporization point of water [34]. The design challenges and safety concerns associated with using such a material are numerous, making them an uncommon choice for solar thermal applications. That is not to say salt hydrates don't have a place in solar thermal energy

storage applications, just that the practical concerns of using them hasn't been outweighed by the amount of simpler system yet to be investigated.

Anhydrous salt media have similar thermal characteristics to hydrated media: they have a favorable energy storage to volume ratios, and are widely available. However, they come with a host of engineering challenges, principally, their thermal conductivity. It is considerably lower than the hydrated media; however, the added benefits of phase stability, simplified containerization and material cost makes addressing issues surrounding their thermal conductivity a worthwhile engineering endeavor. Of the numerous anhydrous salt media explored within the desired cooking range of 100 – 300 °C, the 40%wt KNO_3 60%wt $NaNO_3$ (solar salt) consistently appeared having the greatest ratio of cost to energy storage density. The material's properties are noted in Table 1 [35] and are used for all experiments in this study.

Table 1: Experimental material properties [35]

Solar Salts	
Kinematic viscosity (ν)	3.59e-06 m^2/s
Thermal diffusivity (α)	1.500e-07 m^2/s
Latent heat	145.9 kJ/kg
Prandtl number	23.95
Grashof number	1.712e8
Stefan number	0.797
Melting temperature	221 °C
Specific heat (C_p)	1550 J/kgK
Density (ρ)	1980 kg/m^3
Thermal conductivity (k)	.460 W/mK
Thermal expansion (β)	.0003748 $°C^{-1}$

Aluminum	
Thermal diffusivity (α)	6.65e-05 m^2/s
Specific heat (C_p)	893 J/kgK
Density (ρ)	2730 kg/m^3
Thermal conductivity (k)	162 W/mK

Chapter III – Experimental Methods

3.1 Test Setup

Using the test setup shown in Figure 2(a), 650 grams of solar salt melt and solidify inside of an aluminum enclosure and are observed using thermal measurement devices. Two separate test cases are explored by bottom heating the enclosure using a hot plate: one system utilizes heat conduction enhancement and another does not use heat conduction enhancement, they are referred to as the fin and no fin test cases.

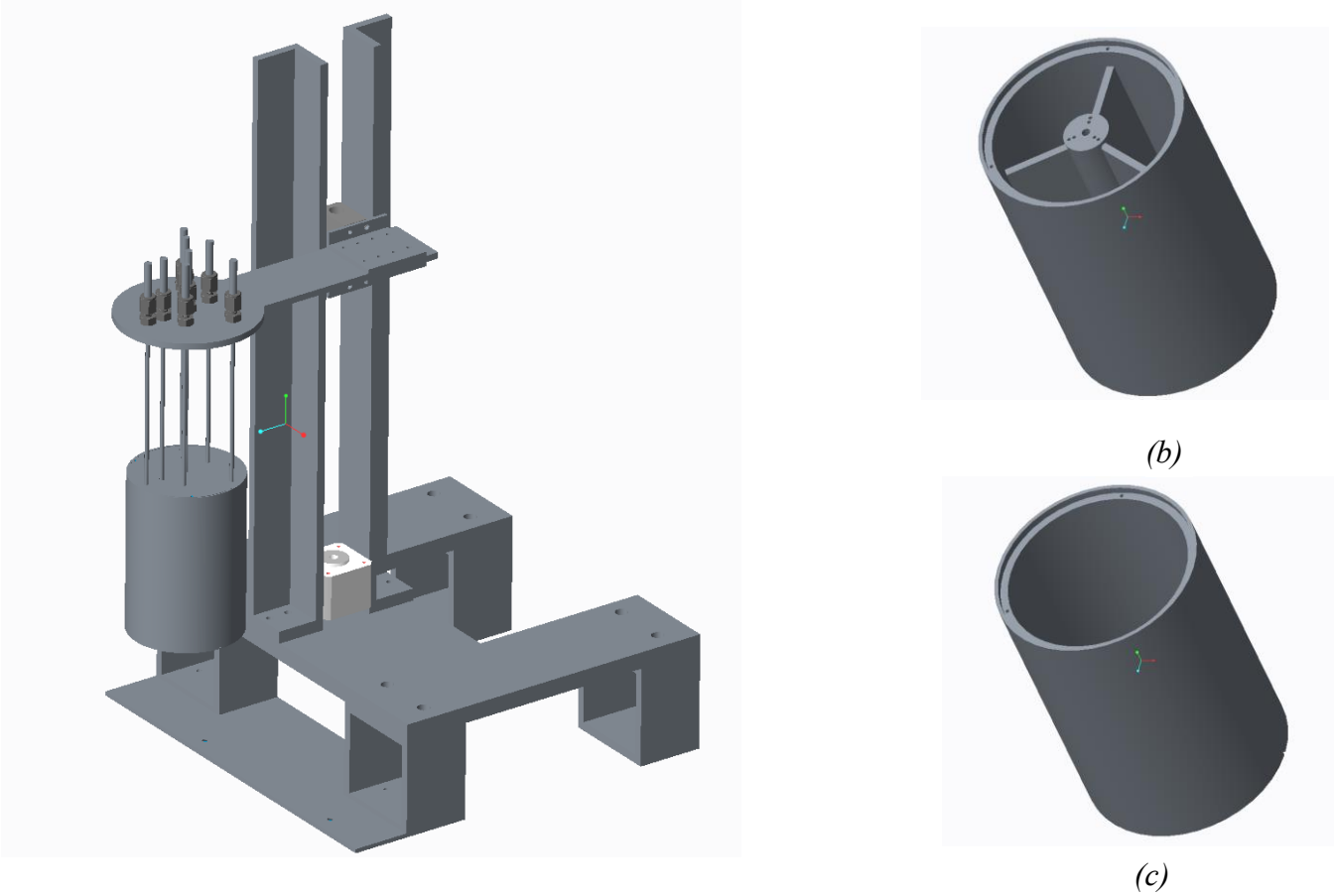

(b)

(c)

Figure 2: (x -blue, y-red, z-green) Experimental test stand depicted without heating source. Test stand is comprised of, test frame, heat source centering plate, traverse frame, carriage brackets; traverse motor, TC holding plate. (b) Experimental test enclosure with fins. (c) Experimental test enclosure without fins.

The first test case, shown in Figure 2(b), utilizes heat conduction enhancement by fitting a 3 fin aluminum heat sink to the inside surface of the bottom of the enclosure. The fin arrangement is custom made using a 5-axis CNC. The CNC machined a 4.125”x .75” OD 6061 aluminum rod resulting in the part shown in Figure 3; this part functions as the core of the insert, holding 3 vertical flat plates. This part has three primary design features; first, the part has milled slots to create an interference fit with the flat plates. This allows for simple manufacturing and the ability to test multiple fin types. Second, a 3.5” blind hole, concentric about the center, fits a temperature probe. This allows for the observation of temperature change in the center of the fin arrangement. Third, six tapped holes at the top surface of the rod allow six 1-72X0.25” hex set screws to apply pressure to top of the inserted fins. This feature serves to reduce contact resistance at the mating surface of the fins and the bottom inside surface of the chamber; additionally, they stabilize the arrangement during thermal cycling.

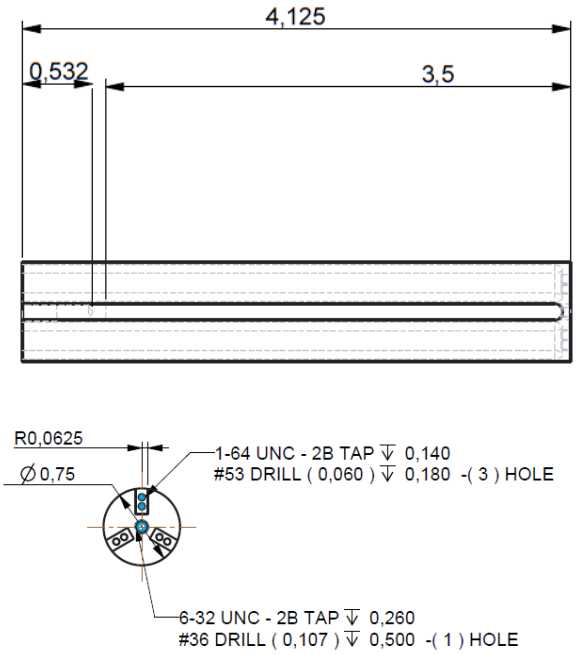

Figure 3: Core dimensions (a) front view showing slotted pockets (b) top view showing set screw dimensions and placement.

The enclosure and the fin arrangement mate using a 10-24x.75” 316 stainless steel (SS) cup-point set screw, concentric about the inside surface and fin arrangement centers. Note, a SS super heli-coil fastener was set flush to the inside surface of the enclosure so the 10-24 SS set screw could mate securely with the aluminum. Previous testing showed that the different rates of thermal expansion between the aluminum enclosure and SS fastener would cause the threads to shear away from the container. The second test case did not utilize heat conduction enhancement. The enclosure was fitted with a lid that allowed for a tight clearance fit of the temperature probes and aided in their positioning. The lid was fixed to the enclosure via 3 1-72x .25” SS UNC hex screws. The enclosure shown in Figure 4 shows a detailed view of the arrangement. The relative mass of each component is displayed in Table 2.

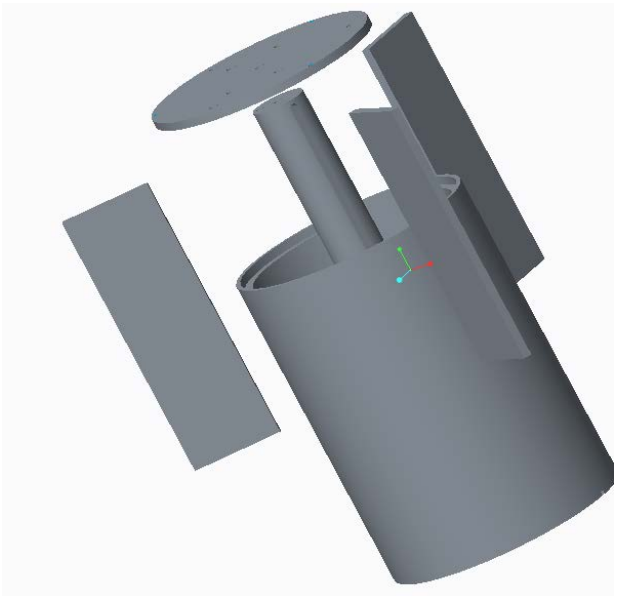

Figure 4: Exploded view of experimental enclosure displaying fins, core, top cap and enclosure.

Table 2: Component count for test enclosure.

Item	**Quantity**	**Mass**
Enclosure	x1	506 g
Fin	x1	28.4g
Core	x1	61.4g
Top Cap	x1	45.2g

3” thick fiberglass insulation is applied to the enclosure’s external wall to reduce heat loss during charging and discharging. A constant heat flux, applied through the external bottom surface of the enclosure brings energy into the system. The heat rate was set to 456 watts using a fisher

electronics hot plate. A variac and Watt's Up watt meter control and log the system's energy input.

Thermal phenomena are observed using an array of 1/8" stainless steel, grounded, OMEGA TJ-36x thermocouples (TC). The TC's are fastened to the TC holding plate, show in Figure 5, using NPT Yor-Loks with SS ferrules. The 2-D configuration, displayed in Figure 6(a,b), shows the locations of the TC insertion points. Each TC tip lies within the same 2-D plane as to have each TC observe a 2-D temperature field at any axial position.

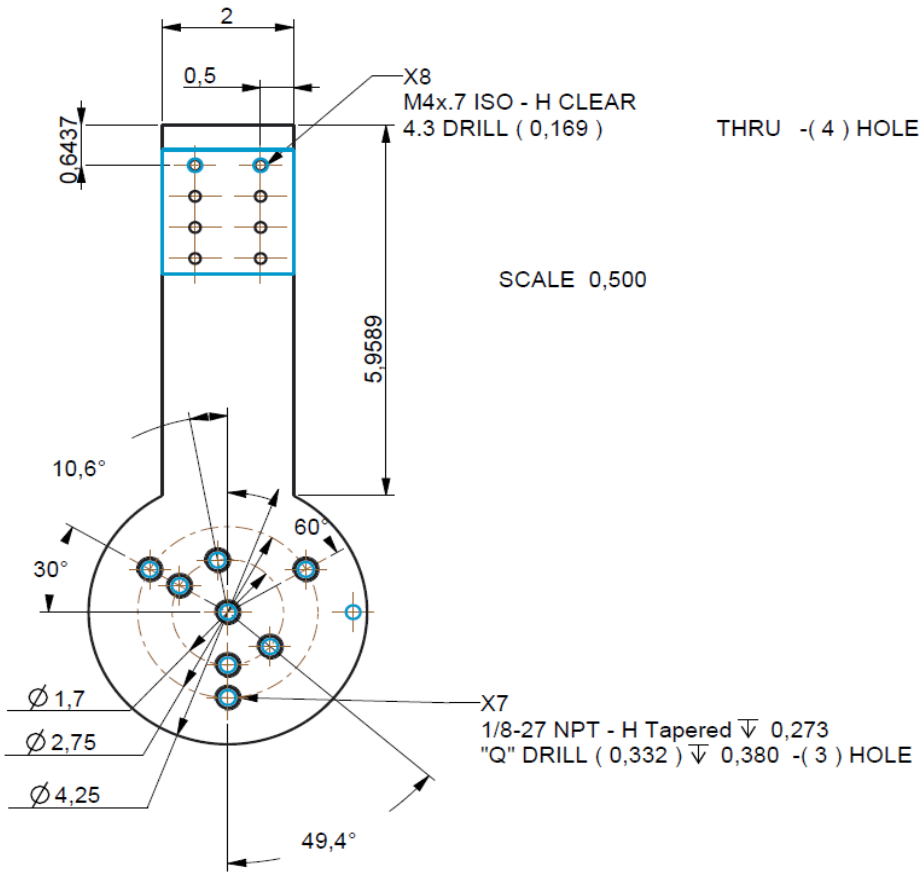

Figure 5: TC holding plate shows threaded fasting holes used to mate plate to traverse and yor-loks to surface of TC holding plate.

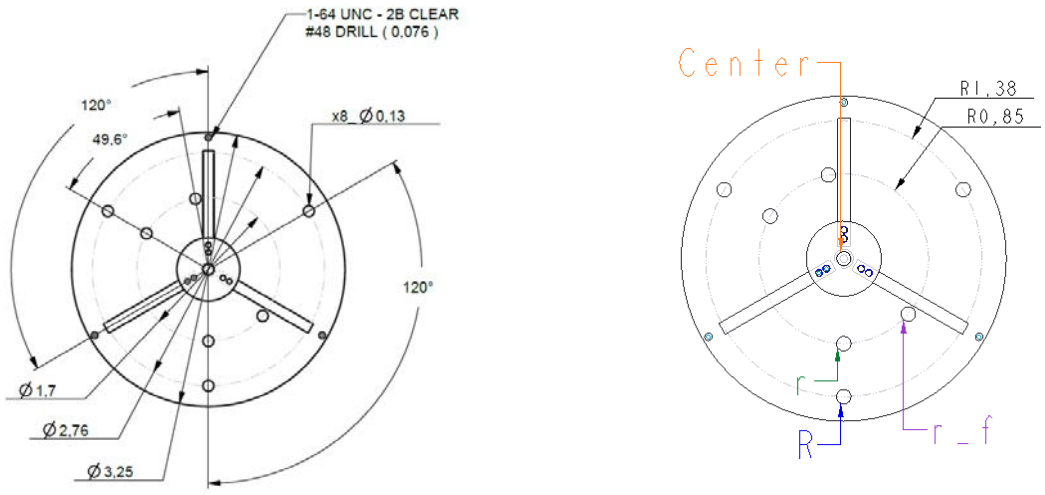

Figure 6(a,b): (a) show the dimensions of the enclosure and thermal observation positions. (b) Provides Identifiers to thermal observation positions for use of identification and description. The holes along the midline of the fin, coplanar with the inside surface of the rim of the enclosure, are the fastener holes used to secure the top lid to the enclosure.

Using a Hayden Kirk linear drive system powered by a ST-5 Applied Motions Driver and controlled using LABVIEW, the TCs are traversed to the three axial locations shown in Figure 7. The intention of selecting locations at the top, middle and bottom of the enclosure is to collect data that will provide an axial thermal profile. The thermocouple carriage was traversed at 25,000 step/rev with a supplied frequency of 10,000hz. The lead screw had a pitch distance of .0625in (.0015875 m). The azimuthal and radial TCs sampled the 2-D temperature field at 1Hz using a NI 6320 PCIe and 9212 DAQ cards.

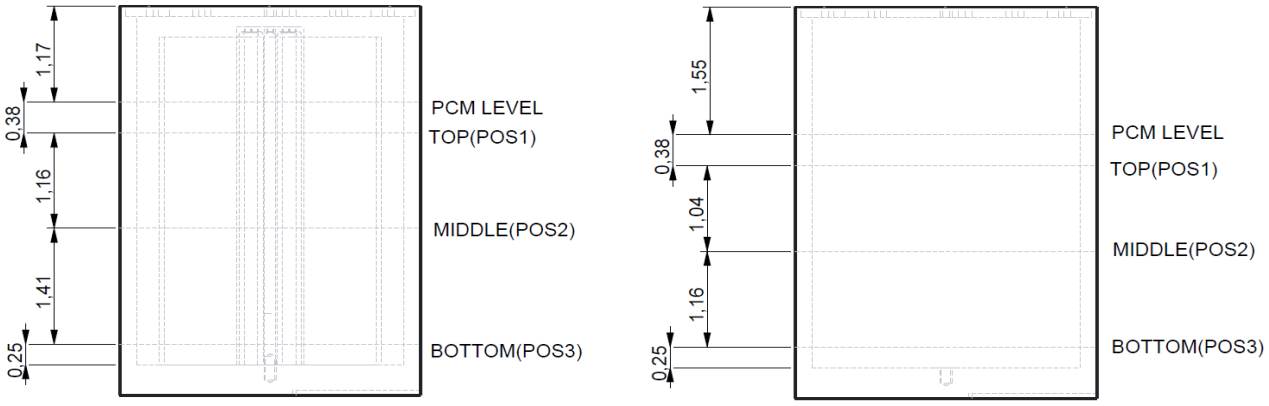

Figure 7(a,b): Shows TC sampling positions in both the finned test case (a) and the no-fin test case (b)

The thermal observation levels were chosen as follows: 0.375 in (.009525 m) below the PCM level (top), half way between the top of the PCM level and the bottom inside surface of the enclosure (middle) and 0.25 in (.006350 m) from the inside bottom surface of the enclosure (bottom). The salt height was determined using the linear stepping traverse. A distilled version of the experimental test setup is shown in Figure 8.

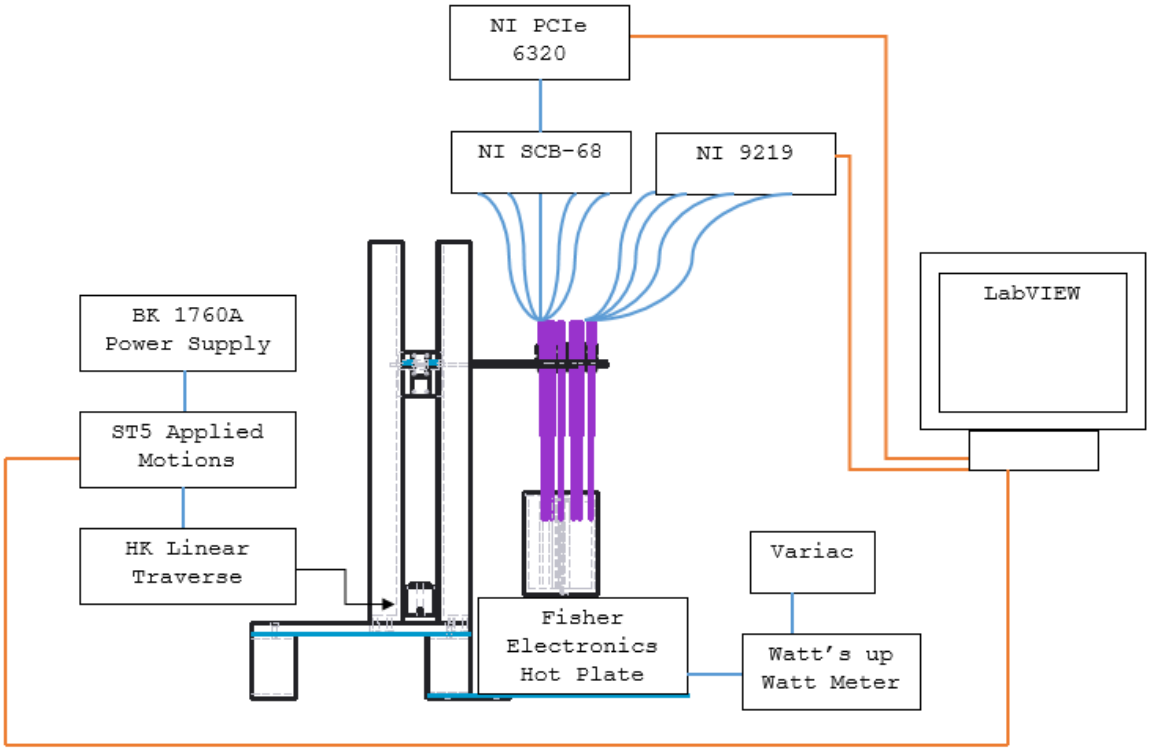

Figure 8: Experimental schematic detailing instrumentation and their respective configuration. Orange lines represent components in direct communication with the PC, blue lines indicate components in communication with each other.

3.2 Procedure

Constituent components of 40%wt KNO_3 and 60%wt $NaNO_3$ are first weighed, then twice ground using an Emperium mill grinder. Afterwards, the salts are left to dry for 8 hours at 100 ºC to remove any moisture. Proceeding moisture removal, the sample is poured into the enclosure and brought 350 ºC to ensure the salt mixture fully melts. The sample is left at this temperature for 4 hours to ensure a homogenous solution is established. After the salts re-solidify and return to room temperature experiments begin.

Energy is supplied to the hot plate at 456 watts until the average temperature of the 2-D temperature field is 300 ºC. Five trials are conducted at each position. Each experiment runs for 12 hours recording data through the melt and solidification of the materials. After trials conclude for one position, the system is brought to a liquid state so the thermocouples can traverse to the next position. The system returns to the environmental temperature before subsequent trials are conducted. The finned case is the first test case to undergo experiments. The repeated sampling of axisymmetric locations, while varying the instrumentation count in each section, was used to investigate the effects of the measurement system on the experiment. Comparing the test cases against one another allowed for the analysis of conduction enhancement on thermal diffusion. Additionally, the salts for the first test case are used in the second test case. Simulations are validated by placing temperature probes at the same locations in the domain space and comparing the results.

Chapter IV – Results and Discussion

Experiments are designed at $1/8^{th}$ scale to reduce the amount of experimental materials, time and to simplify the domain for computations. The experiments comparatively quantify the effect of conduction enhancement on thermal transport; as well as, explore the effect of the measurement system on the accuracy of data recorded. The subsections are divided accordingly: conduction enhancement and system performance, evaluation of measurement method and computational simulations.

Analyses are comprehensive of the two test cases described in the methods section. Results present phase change characteristic curves by separating data into their independent heating and cooling phases.

4.1 Conduction enhancement and system performance

4.1.1 Thermal Characteristics

As previously described in chapter 3, three axial and four azimuthal locations comprise observation points for data acquisition. The arrangement of temperature probes, and method used for data collection, considers spatial and temporal variance in a cylindrical aluminum enclosure. Using these data, investigating the effect of conduction enhancement on system performance is possible.

Graphing the change in temperature versus time generates a 'thermal characteristic' plot; it features general trends and tendencies of the system during heating and cooling. The experimental test cases will be analyzed individually. In a like manner, the charging and discharging phases will be analyzed individually for each test case. First, examining the finned case's thermal characteristic plots during the heating phase, displayed in Figure 9(a-c), shows significant features such as the solid – solid phase change, first detection of the melt front and its passing.

First, as observed in Figure 9, the enclosure's horizontal cross-section exhibits a uniform temperature profile. At any point in time and at all axial positions, the TC's vary in temperature by no more than 12 ^{o}C. This is an important point— the fin arrangement is acting as an extension of the heat-receiving surface. This means that the salts are experiencing heat spreading throughout the trial.

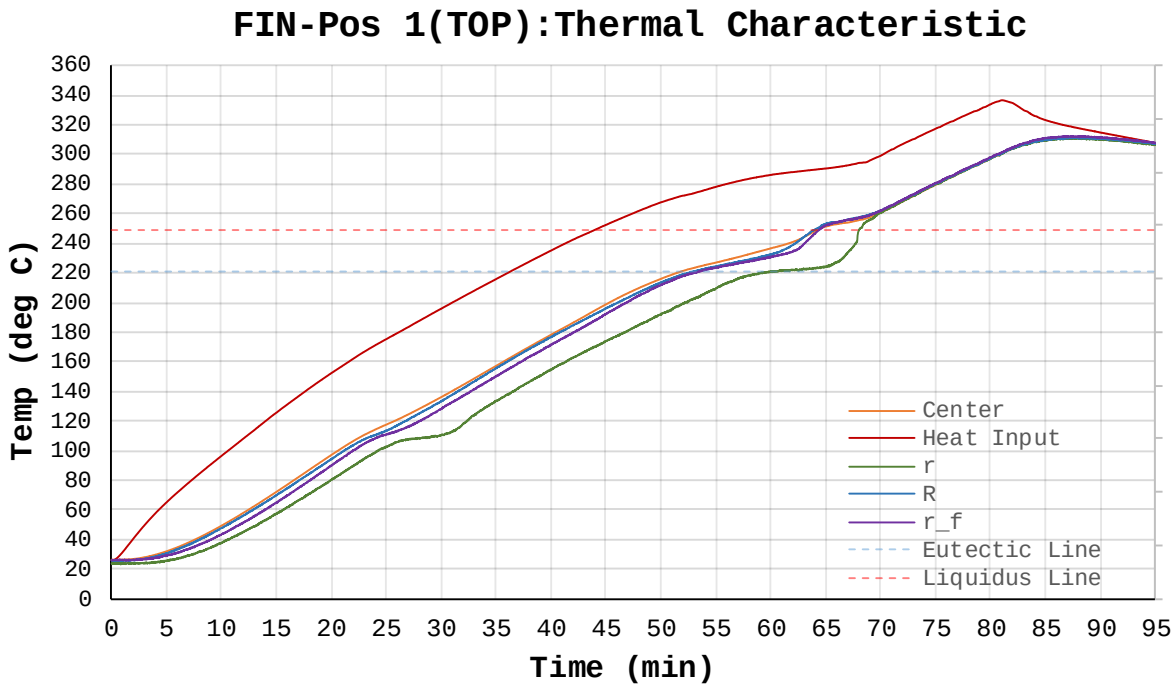

(a)

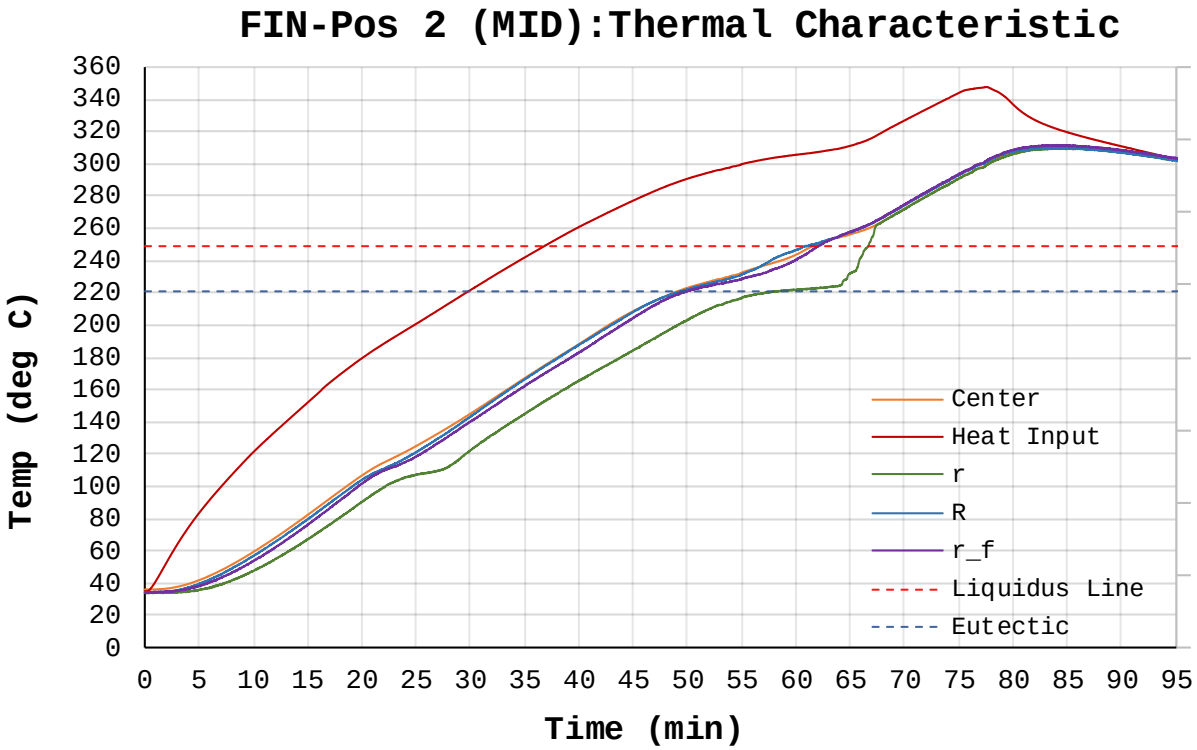

(b)

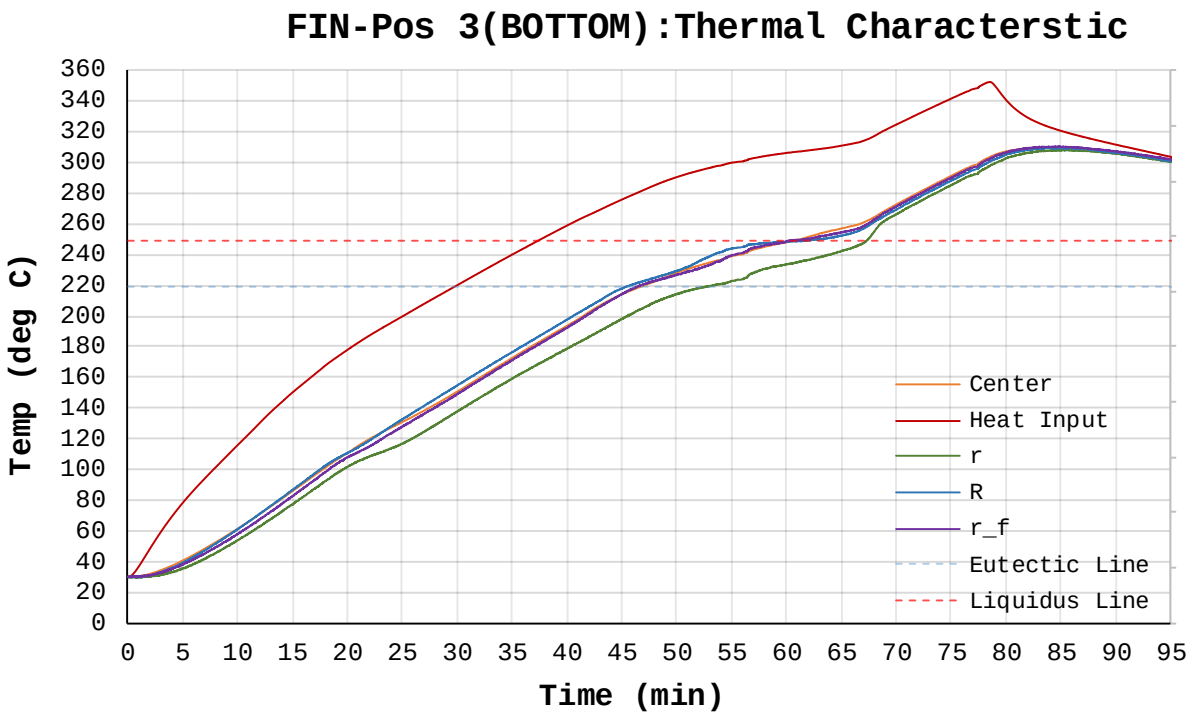

(c)

Figure 9(a,b,c): Thermal characteristic plots disply temperature change at top, middle and bottom respectively in the finned test case. Only the heating phase is displayed.

Close examination of Figure 9 shows 'R' registers a marginally higher temperature over 'r_f' due to the geometry of the enclosure. 'R's' tips reside .003175m (.125 inches) away from the interior wall of the enclosure and 'r_f' resides .003175m (.125 inches) away from the fin. The contact area of the wall (.001206m^2 or 1.87in^2) is greater when compared to the contact area the fin arrangement (.000523m^2 or 0.811in^2); therefore, 'R' experiences higher temperatures than 'r_f' due to an inherently larger temperature gradient. More importantly, results show the walls and fins of the enclosure heat at a faster rate than the TC located at 'r'. This yields two important results: first, this means that the solid salts that contact the walls and fins will transition more quickly than the salts residing in between. Secondly, because 'r' is closer to thermal equilibrium at any point in time relative to the other TC's due to the salts insulating properties, 'r' can be used to more easily identify the eutectic and liquidus temperatures.

The transition points become salient after overlaying the first derivative of the thermal characteristic plot atop itself. The first detection of a phase transition occurs at ~23 minutes, corresponding to the S-S phase change temperature of 107 ºC and again at ~60 minutes when 'r' exceeds the eutectic temperature of 219 ºC. Afterward, the salt moves in to a two-phase fluid region characteristic of the latent heat of fusion. In the two-phase region, conventionally called the "mushy zone", the intermolecular forces that bind the solution in a solid state begin attenuating as the energy content in the enclosure continues to increase. As the solution continues to heat, the ratio of liquid to solid mass inside of the two-phase region established a positive feedback loop in which the addition of heat expedites the heat flux seen by the fluid inducing greater convection and conduction heat spread. The mushy zone's solid to liquid fraction continues to decrease until a fully liquid state is established at 249 ºC.

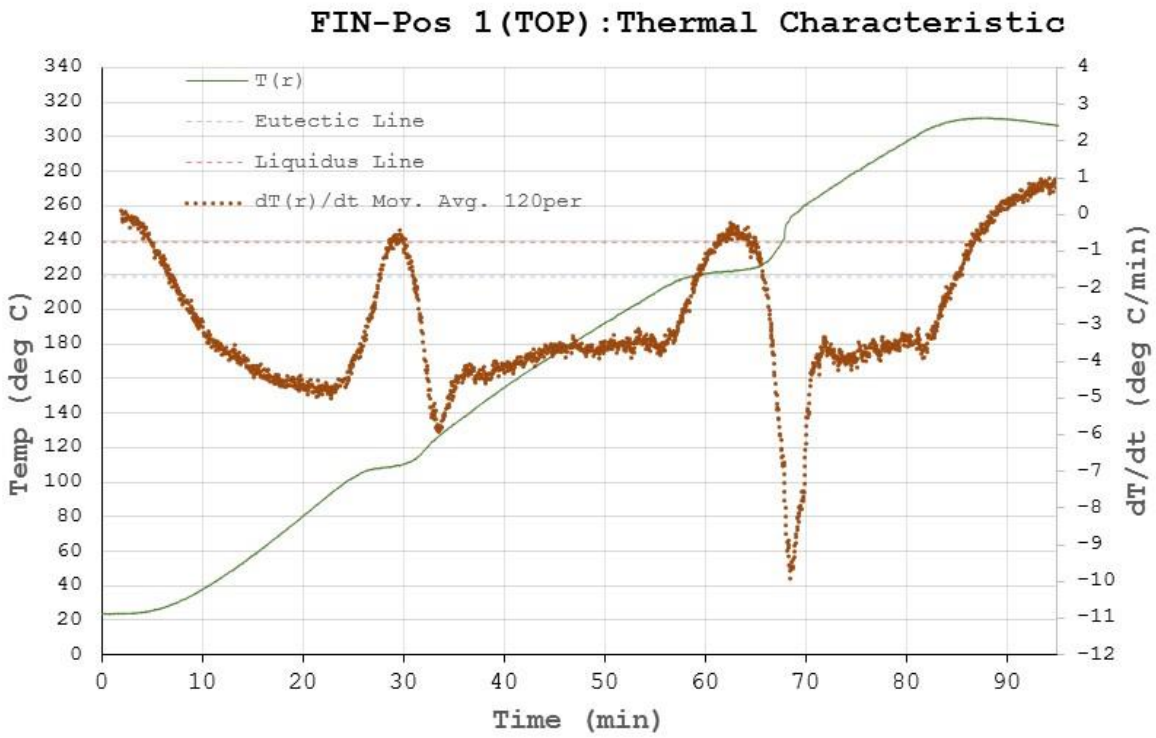

Figure 10: TC 'r' plotted at the top position with the heat rate plot layed atop of it..

A secondary result is found by analyzing the melt data. By approximating when the thermal characteristic lines reach the eutectic and liquidus temperatures, shown in Table 3(b), two features stand out. First, the TC's at the top position reach the transition temperature approximately 4 minutes sooner than the TC's at the middle position. This indicates that the top of the salts melt before the middle. In fact, at each azimuthal position, 'R', 'r_f' and 'center, reach the transition temperatures well before 'r'. This implies that convective cells grow along the walls first then liquefy the top of the salt mass; then solid to liquid fraction continues to decrease all fronts of the solid mass until the enclosure reaches a full liquid state. TC 'r' is the last to melt at all axial positions.

Table 3(a,b): Time taken for each TC at a given axial location to reach the eutectic or liquidus temperatures.

(a)

Melt					
Eutectic Line					
Position	Test Case	Top (min)	Middle (min)	Bottom (min)	Average
C	Fin	55	55	49	53
	No Fin	59	62	47	56
R	Fin	52	52	49	51
	No Fin	46	45	39	43.33333333
r	Fin	61	64	56	60.33333333
	No Fin	55	59	50	54.66666667
r_f	Fin	56	52	49	52.33333333

(b)

Melt					
Liquidus Line					
Position	Test Case	Top (min)	Middle (min)	Bottom (min)	Average
C	Fin	64	62	61	62.33333333
	No Fin	60	64	51	58.33333333
R	Fin	64	62	61	62.33333333
	No Fin	52	51	46	49.66666667
r	Fin	68	67	67	67.33333333
	No Fin	58	61	56	58.33333333
r_f	Fin	65	62	61	62.66666667

The discharge plots offer fewer distinguishing characteristics than the charging plots do. Shown in Figure 11 (a-c), two main features emerge: first, the LHES material reaches the liquidus line sooner as the temperature probes move from the top to the bottom position. This is one indication that heat may be lost more rapidly more rapidly from the bottom of the enclosure than it is from the top.

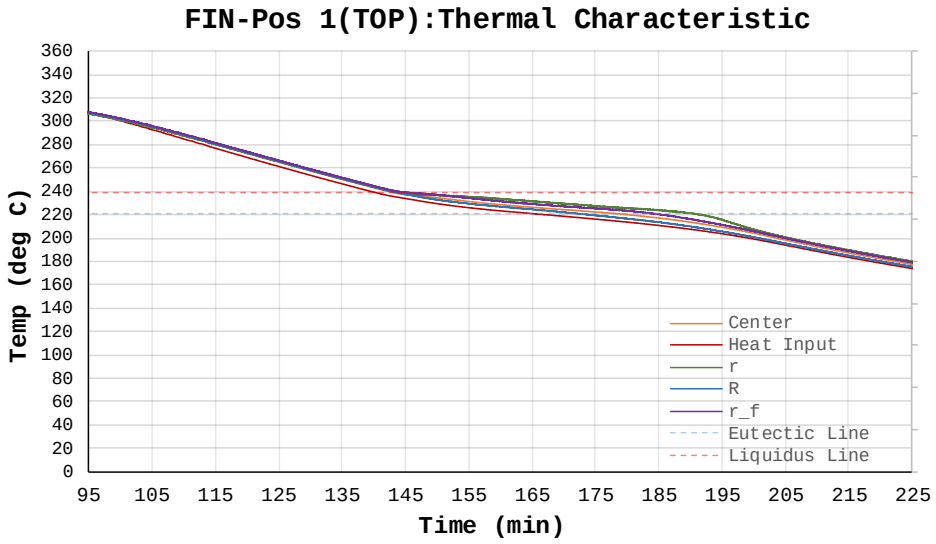

(a)

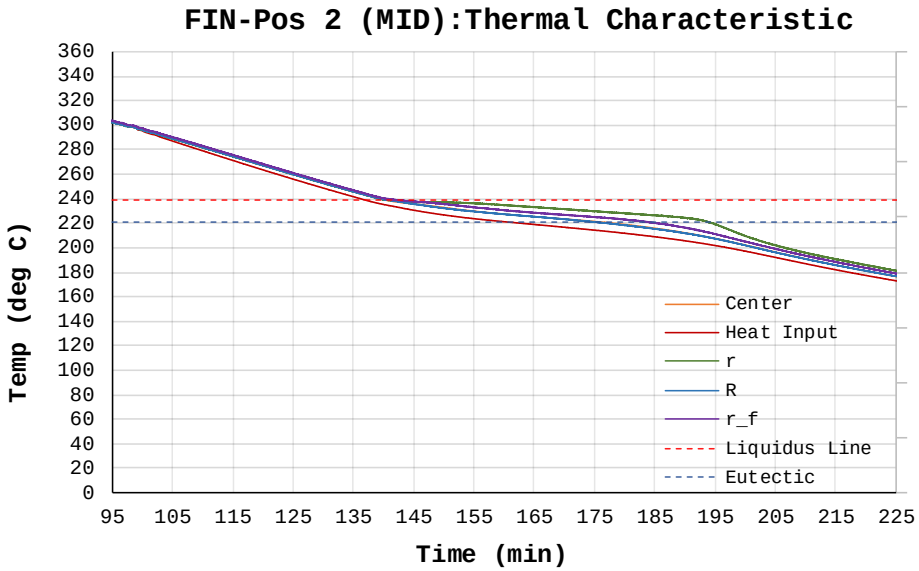

(b)

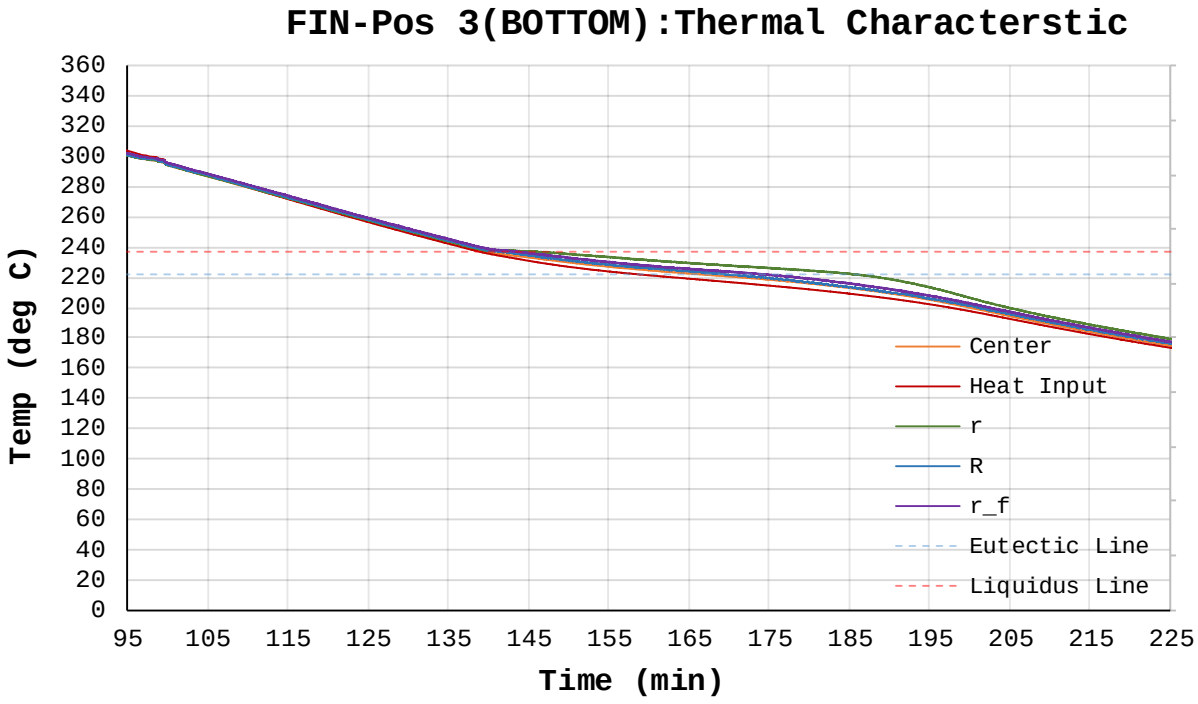

(c)

Figure 11(a-c): Fin test case solidification thermal characteristic plots.

Secondly, the probes at each axial and azimuthal position cool at a uniform temperature; where T(r,Θ) = constant, until the PCM reaches the liquidus line at 239 ºC. After this point, thermal stratification increases inside the enclosure until reaching the eutectic temperature at 219 ºC. Spatially, the salt experiences different rates of solidification as observed by the TCs. Once this process is completed, the enclosure cools uniformly until it reaches ambient temperatures.

Before explaining the no fin data, an important digression needs to be made about the eutectic and liquidus temperatures. During both melting and solidification the eutectic temperature of 219

ºC has shown to be consistent with the literature; however, careful observation of the thermal characteristic and heat rate plots show the liquidus temperature reflects clear signs of hysteresis. The thermal characteristic shows two different values for the liquidus temperature: 249 ºC for charging and 239 ºC for discharging and the heat rate plots show clear inflections that correspond with a change in state at these temperatures.

With few scientist writing on the subject, thermal hysteresis is uncommonly discussed in phase change material literature. Despite, one study using Differential Scanning Calorimety (DSC) to explore thermal hysteresis in the same off eutectic mixture of Sodium Nitrate and Potassium nitrate (60%$NaNO_3$ 40%KNO_3) used in this research and found an 8 ºC difference between the onset of thermal transitions between heating and cooling, the study was limited to the solid to solid phase change [36]. Finding other studies on the thermal hysteresis in solar salts has proved to be difficult which indicates that there is more to learn about this phenomena and what influences it may have on design optimization. Furthermore, and discussed in greater detail later, only simulations coded to account for thermal hysteresis yielded results that matched the experimental data.

The thermal characteristic curves shown in Figure 12 show greater thermal stratification indicating an uneven distribution of heat. This implies that the development of convective melting must be different than that of the fin case. The data from Figure 12 (c) supports this claim by providing evidence for strong convective cell growth in the beginning of the experiment. As soon as 'Center' crosses the eutectic line, its heat rate increases significantly

relative to ‘R’ or ‘r’, despite ‘center’ and ‘r’ exhibiting near identical thermal characteristics (through the sensible heat phase in the solid portion of the salt). This results in a strong change in heat flux, occurring at ~48 minutes at ‘Center’, noted in Figure 12 (b). ‘Center’ climbs to the eutectic line then drops back below the melting temperature for ~8 minutes. Supported by data collected from ‘r’, the surrounding solid thermal mass is below the eutectic temperature at onset of ‘Center’s change in heat rate; therefore, when the liquid portion of the material is forced through the center of the phase change material, the surrounding medium absorbs its sensible heat and returns the liquid back to its solid state. Distilling this information implies a quick development of a liquid mass at the bottom of the salt.

Moreover, because the aluminum side walls short circuit the heat path through the phase change material it ensures that the walls heat quickly. The quick heating of the walls is an important part of generating convection cells that contact the length of the salt. Support for this is found by analyzing the melt data shown in Table 3. The TC’s at the top position reach the transition temperature approximately 4 minutes sooner than the TC’s at the middle position. In a like manner of the fin case, this indicates that the top of the salts melt before the middle. However, in the no-fin case, the presence of top melting is less intuitive given that there are no direct means of transporting heat to the top level. The melting of salt at the wall/salt interface allows for salt that has melted at the bottom/salt interface to find passage around the solid salt mass and induce further melting from the top. Further support for this idea can be found in Table 3**Error! R eference source not found.**; ‘R’ and ‘r’ reach transition temperatures well before ‘center’, except at the bottom position.

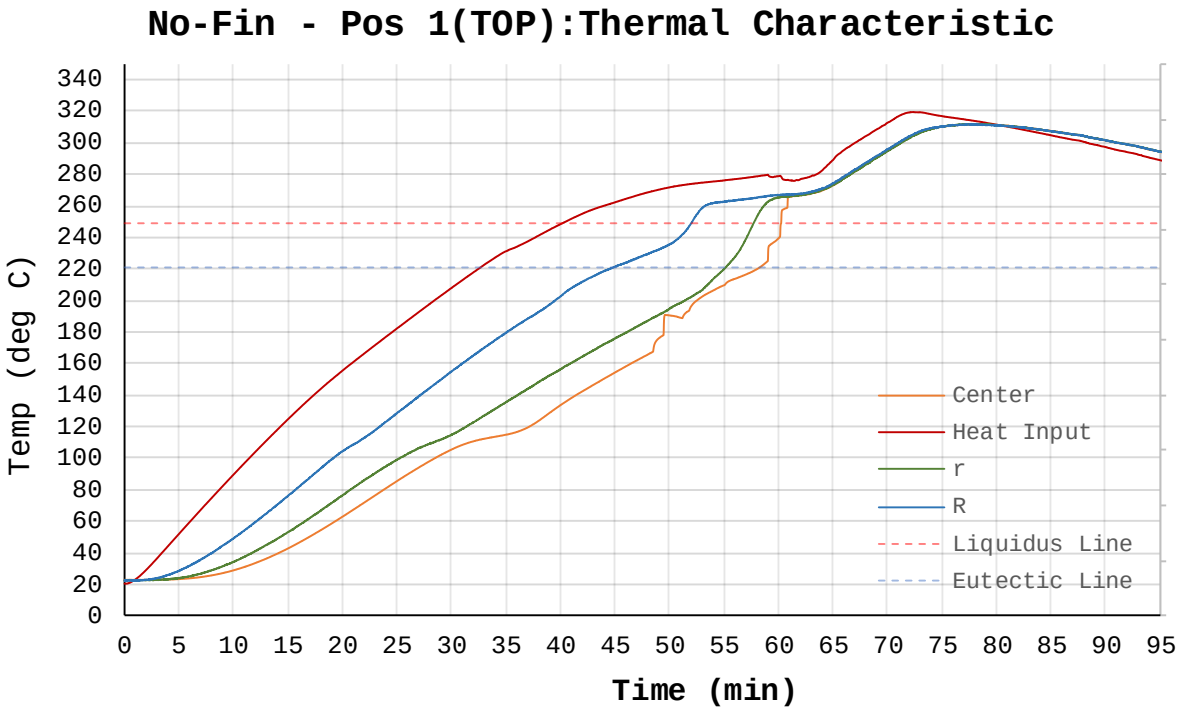

(a)

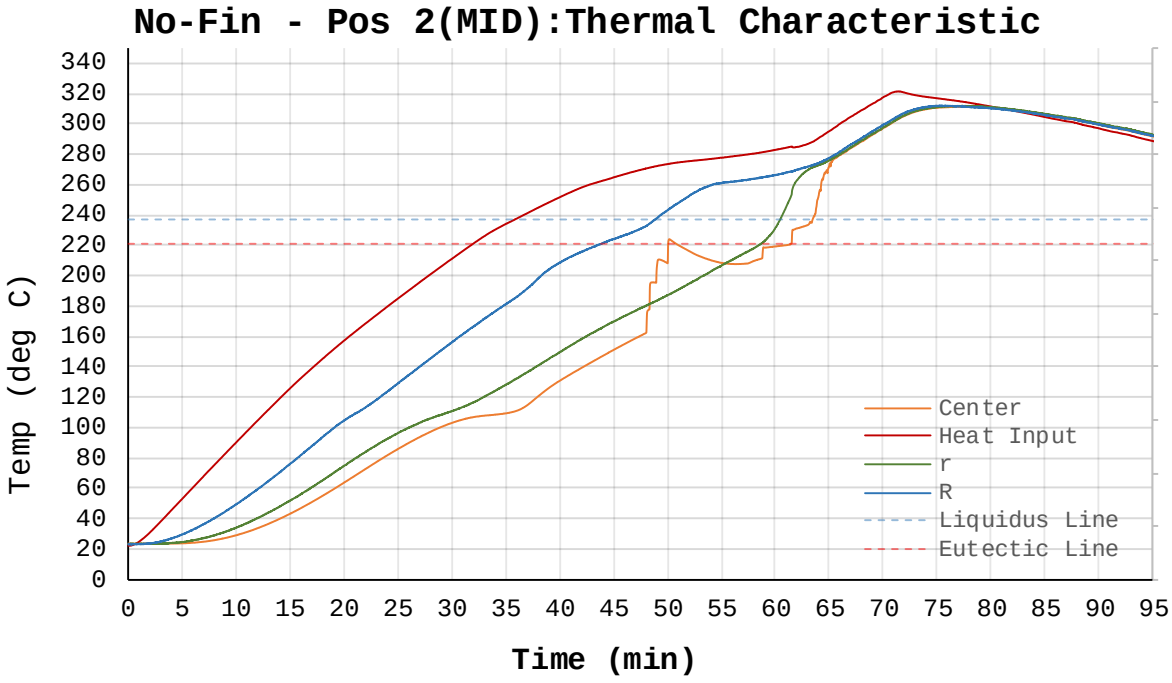

(b)

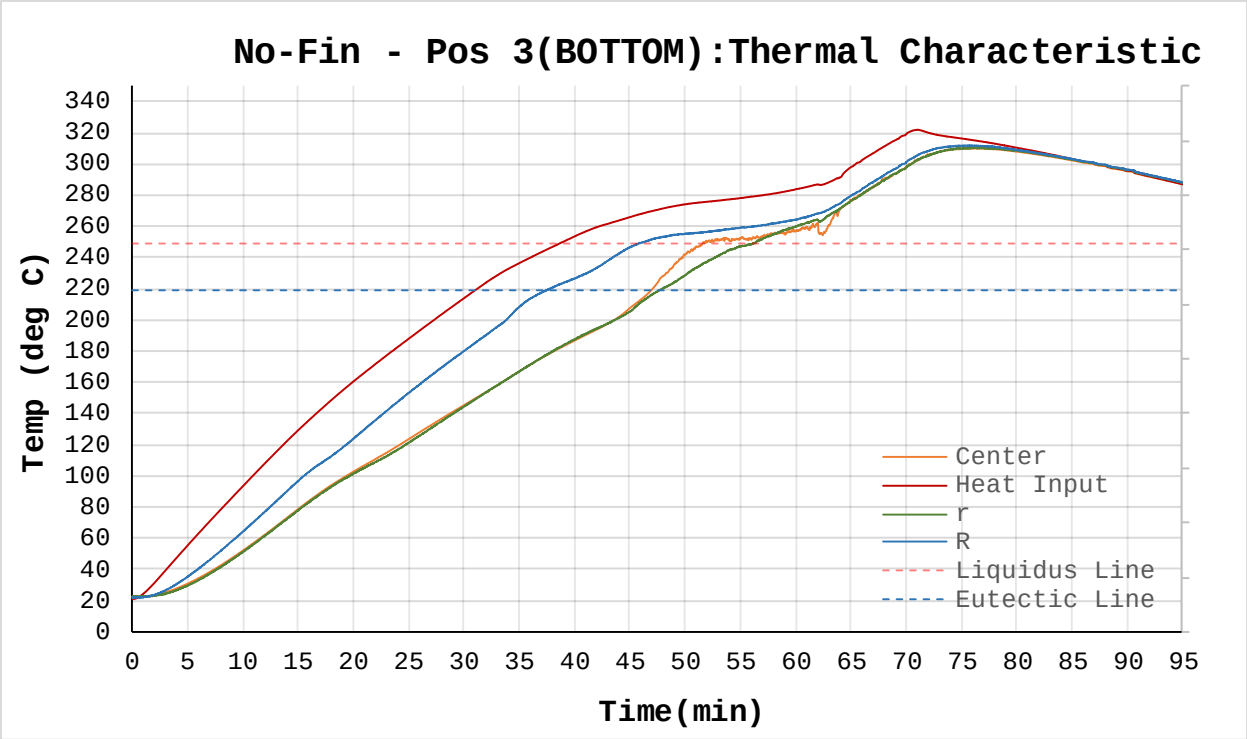

(c)

Figure 12 (a-c): Displays the thermal characteristic of heating for the no fin cases with position 1 shown in (a) position 2 shown in (b) and position 3 shown in (c). 'r_f' is removed as it records the same temperature as 'r'.

Shown in Figure 13, the no finned solidification plots exhibits near identical features to that of the finned cases. The PCM reaches the liquidus line sooner as the temperature probes move from the top position to the bottom position, the temperature probes at each axial and azimuthal position cool at a uniform temperature and the azimuthal temperature probes, for any given Z, reach the eutectic line in the reverse order from which they melt.

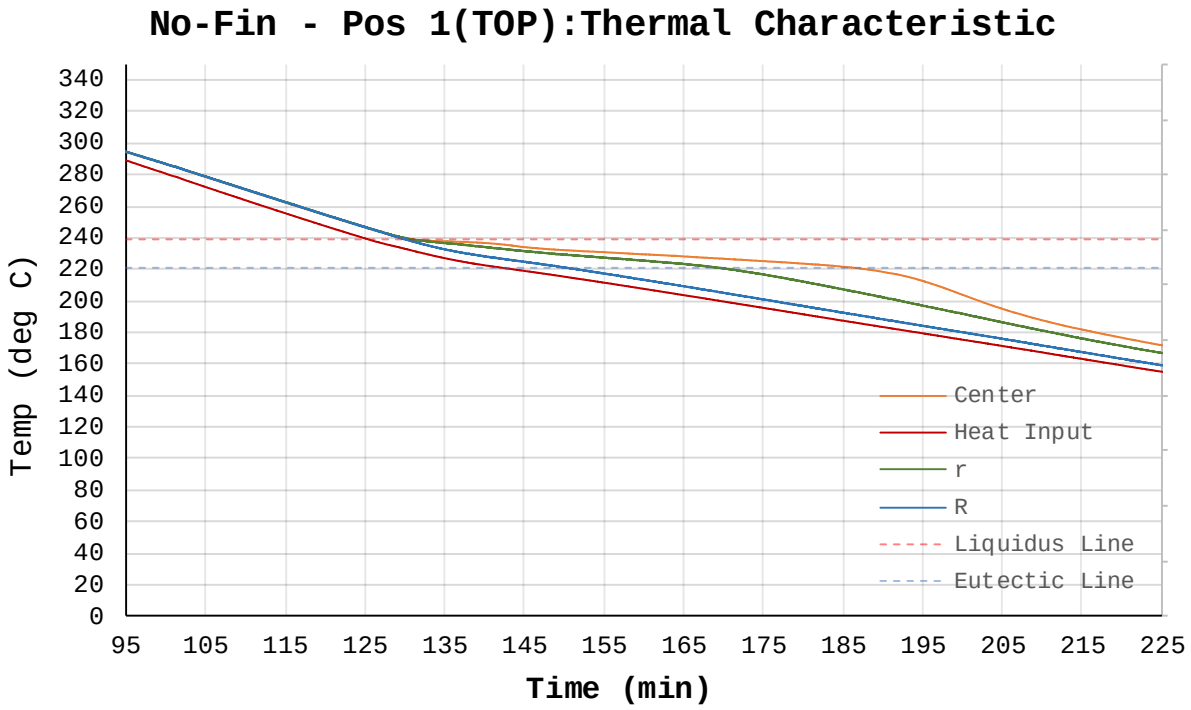

(a)

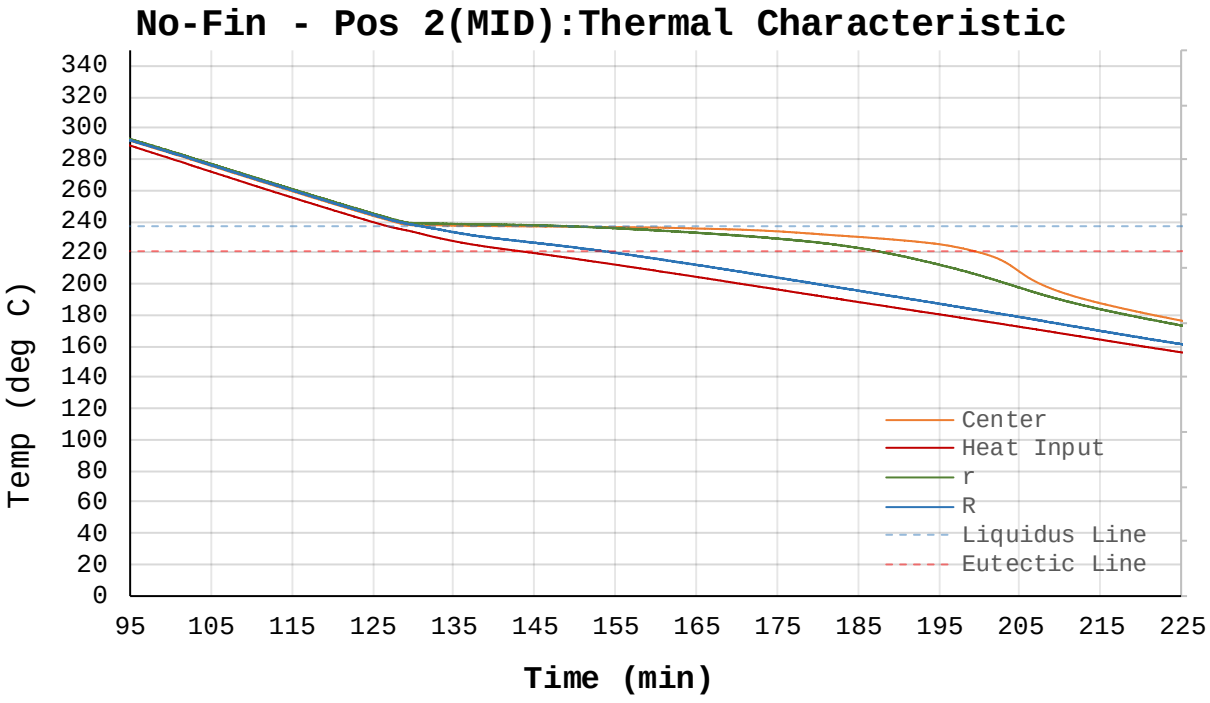

(b)

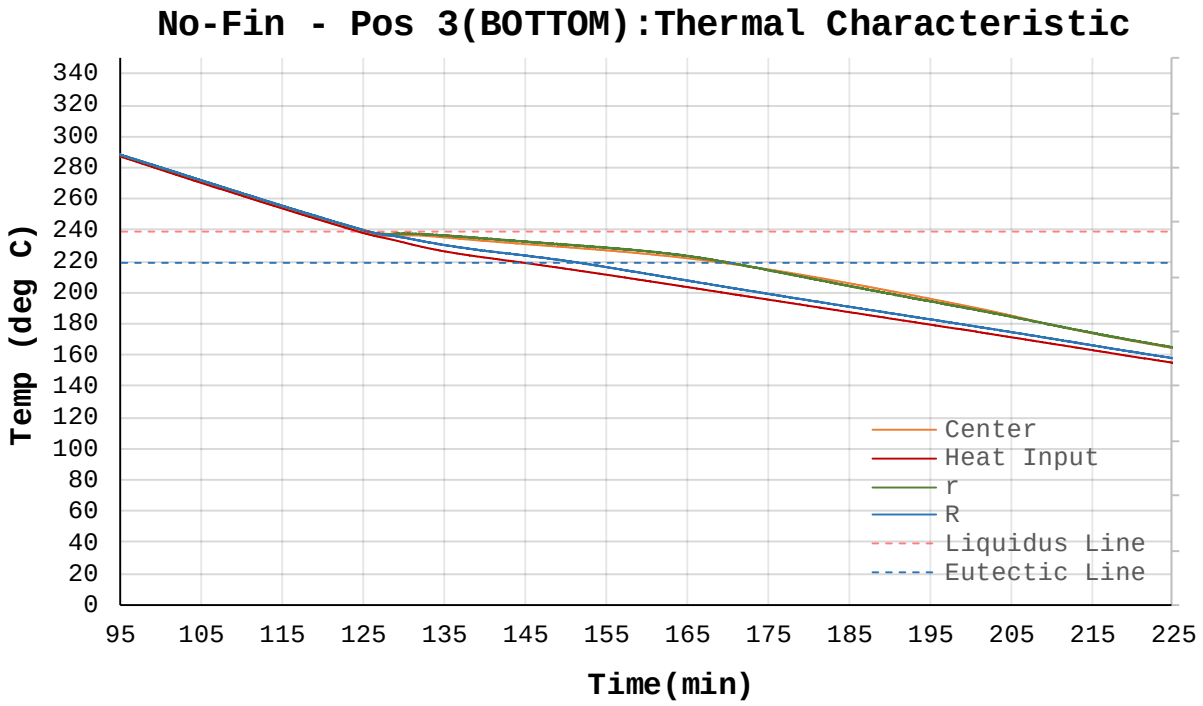

(c)

Figure 13(a-c): Solidification thermal characteristic plots for the no fin case.

While 'center' and 'r' cool uniformly through the phase transition, Figure 13 shows 'R' experiences a different heat rate and lower temperatures. Moreover, 'R's thermal characteristic shares the same shape as 'heat input'. Without a heat sink, the enclosure relies on the walls to conduct heat out through the top or and bottom boundaries during melt and solidification. That being said, the data seems to imply that heat is most readily lost through the bottom of the enclosure as opposed to the top.

Measured from the time in which the energy supply is termianted from the experiment, the data shown in Table 4 reflects the liquidus temperature being reached at the bottom of the enclosure first, which means the bottom the enclosure solidifies first.

Table 4 (a,b): Time at which the material reaches the liquidus or eutectic temperatures.

(a)

Solidification					
Liquidus Line					
Position	Test Case	Top (min)	Middle (min)	Bottom (min)	Average
C	Fin	55	56	52	54.33333333
	No Fin	52	51	49	50.66666667
R	Fin	57	56	55	56
	No Fin	52	52	48	50.66666667
r	Fin	55	56	55	55.33333333
	No Fin	52	52	48	50.66666667
r_f	Fin	58	56	55	56.33333333

(b)

Solidification					
Eutectic Line					
Position	Test Case	Top (min)	Middle (min)	Bottom (min)	Average
C	Fin	95	91	89	91.66666667
	No Fin	109	122	94	108.3333333
R	Fin	88	91	89	89.33333333
	No Fin	73	76	74	74.33333333
r	Fin	105	109	105	106.3333333
	No Fin	92	109	94	98.33333333
r_f	Fin	98	101	95	98

However, the data also shows the PCM reaches the eutectic temperature at the top before the bottom at locations ‘R’ and ‘r’ by a few minutes. This implies that the bottom cools more quickly while the PCM is in a liquid state; however, as the solid layer begins to grow at the bottom surface the rate of heat transfer decreases. This implies that the solid layer grows more quickly at the bottom inside surface than it does at the top. Additionally, despite the fin case having significantly more mass the no-fin case, the fin case move through the latent heat region during solidification 10 minutes sooner than the no-fin region with heat being extracted from the center of the enclosure 30 minutes sooner than the no-fin case.

Directly comparing the effectiveness of the two designs is difficult as the fin case contains more aluminum than the no-fin case does. However, the experiments show that they both exhibit unique flow qualities. In contrast to the no-fin case, the experiments show the fin case produces a near uniform heat distribution inside the enclosure. This implies greater heat spreading during the conduction dominated heat transfer phase of the experiment. The experiments show the result of these physics occurring: in Figure 9. 'R' and 'r_f' exhibit higher heat fluxes relative to 'r' during the conduction dominated phases of charging; and more importantly, liquefy approximately 4 minutes sooner than 'r'. The figures illustrate that the time taken for 'R', 'center' and 'r_f' to reach the eutectic temperature at the top position is ~8 minutes sooner than the time taken for 'r' to reach the eutectic temperature at the middle position. Observing 'r's thermal characteristic in Figure 9 (b) at the time cited in Table 3 when 'R' and 'r_f' reach the liquidus temperature, the slope of 'r' changes dramatically. This data would suggest that the formation of convection cells that span the length of the solid mass directly influence the rate at which the salts will liquefy.

Contrasting this with the no-fin case the experiments show, at the top position, that 'R' begins liquefying early on where the walls at the top position establish liquid state at ~ 52 minutes and 'center' at ~64 minutes. Additionally, 'R' reaches the liquidus temperature at ~46 minutes in the bottom position, where 'R' reaches the liquidus temperatures simultaneously for top and middle. This suggests that the bottom of the enclosure melts early and contains mostly liquid based sensible heat without the opportunity to spread it effectively until the side walls melt ~10 minutes later. This, in its essence, reveals the effect of conduction enhancement.

4.1.2 Conclusions

In conclusion, the data suggests that that establishment of liquid regions that span the length of the salt mass are correlated with quicker melt times. Even though the no-fin case experiments terminated sooner and established a liquid state sooner, it also took significantly longer to melt its solid salt core after melt had been established. This was evident by observing the no-fin's thermal characteristic. The data showed that the no-fin case was not able to effectively spread its volume of liquid based sensible heat until the side walls melted ~7 minutes after the first detection of melt at the bottom of the enclosure. Comparing this to the fin case, melt was established at the top of the enclosure ~3 after the detection of melt at the bottom. Moreover, the no-fin case took ~9 minutes longer to melt the salts at the top position 'r' than the fin case did. Such melt times suggest that if the fin cased was used at greater scales, it would significantly melt improvements over the no-fin case.

Additionally, despite the fin case having significantly more mass the no-fin case, the fin case moved through the latent heat region, during solidification, 10 minutes sooner than the no-fin region with heat being extracted from the center of the enclosure 30 minutes sooner than the no-fin case. This is due mostly to the fact that the distance between the solid salt core and an aluminum face, in the fin case, reduces the low thermal conductivity effects of the solid salt.

4.2 Evaluation of Measurement System Accuracy

This analysis compares the fin test case's thermal data measurement methods, where measurement method 1 (MM1) provides thermal data as the average of 'R-3' and 'R-4', where 'R-3' and 'R-4' neighbor other equally spaced thermocouples (TC's 'r' and 'r_f'), measurement method 2 (MM2) provides the same thermal data with a single thermocouple and no neighboring thermocouples ('R-7'). Figure 14 identifies the TCs used in this analysis and their positions. Both methods are designed to observe temperature change about the phase change material at position 'R'. The primary goal of this investigation is to determine whether the measurement system presents an effect on the evolution of thermal phenomena.

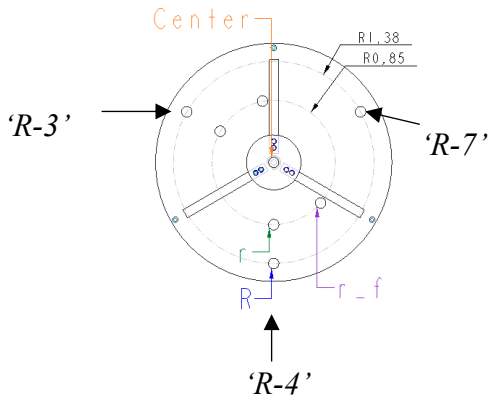

Figure 14: Provides identifiers to thermal observation positions.

Historically, by calculating the product moment correlation coefficient, (r), one can compare two measurement's level of agreement. This involves creating a line of equality and determining if the two measurement methods provide the same results by noting where the points lie. Readily seen in Figure 15 (a-b) is the measurement difference between the two measurement methods that comprise these tests rarely deviate from the line of equality throughout the duration of heating. Figure 15 (b) displays the same trend as Figure 15 (a) with a reduced window showing the interval at which the greatest deviation between the two measurements is expected to occur

(the onset of melt); calculating the correlation coefficient reveals a value of .944. This number would indicate that the measurement systems highly agree.

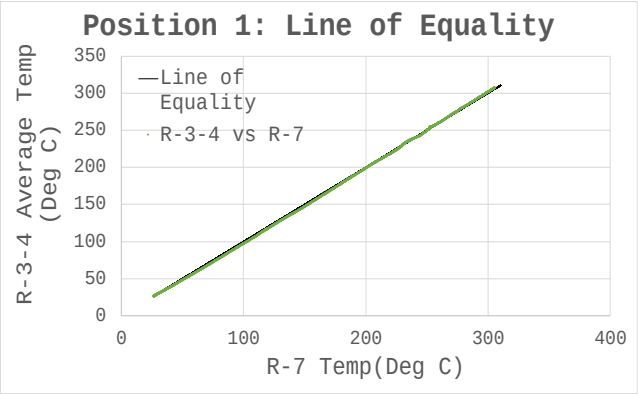

(a)

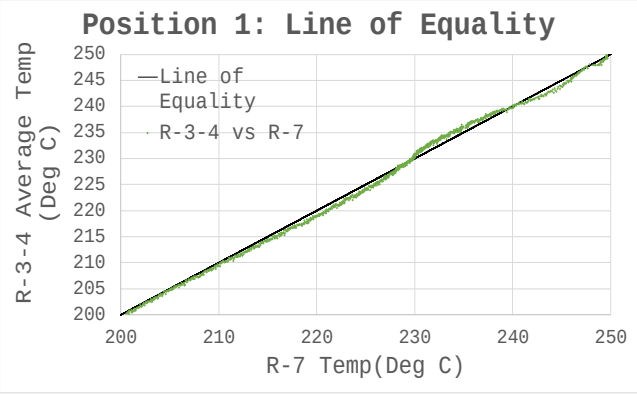

(b)

Figure 15 (a-b): Correlation plots display the line of equality for 'R 3-4' average vs 'R-7'. (a) Displays the entire temperature interval over which data is collected during the melting phase at position 1. (b) Displays a reduced window to show deviation from line of equality during melt.

However, noted by Bland and Altman [37], the correlation coefficient only measures the relationship between the variables not the agreement: perfect correlation exists if the points lie along any straight line where perfect agreement exists if the difference between two measurements lie along a line of equality. As data provided in the later sections will show, this approach fails to capture the magnitude of the agreement. Therefore, Bland and Altman devised a better method for comparing agreement; their method focuses on applying simple statistics to a "plot of the differences between the methods against their mean" (which will be referred to as Bland-Altman plots). This method more readily reveals data points that fall outside an acceptable level of error.

The Bland-Altman plots will be used in conjunction with the frequency distribution plots to first, determine the accuracy of the measurement methods and second to compare their results so the

question of whether the measurement system significantly influences the development of flow behaviors can be asked further. This helps ascertain whether differences experienced by the measurement methods are a function of physical behavior or measurement error. Additionally, their agreement, or lack thereof, stands as an indication of thermal symmetry. To start, the frequency distribution of the measurement difference are analyzed in order to determine which statistical tools to apply. The plots shown in Figure 16 (a-c) display the measurement difference distributions from TC's comprising MM1.

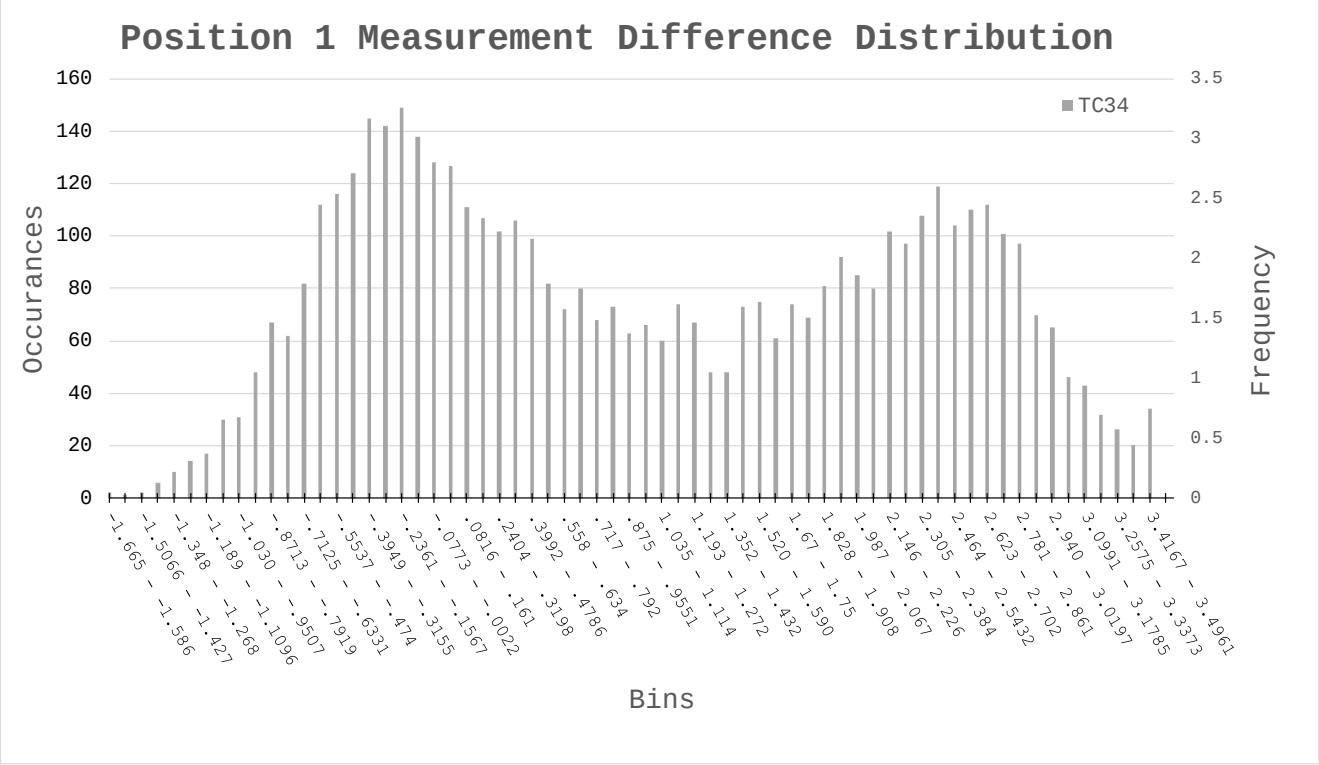

(a)

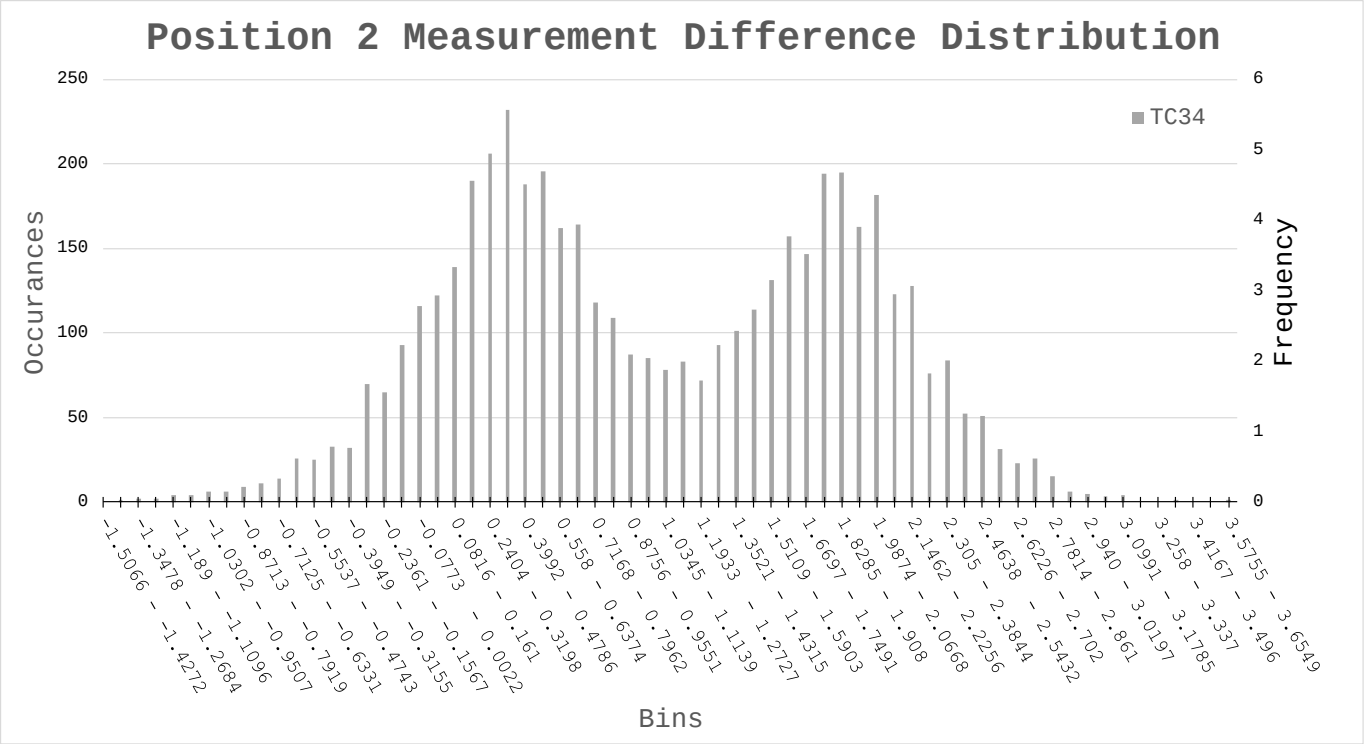

(b)

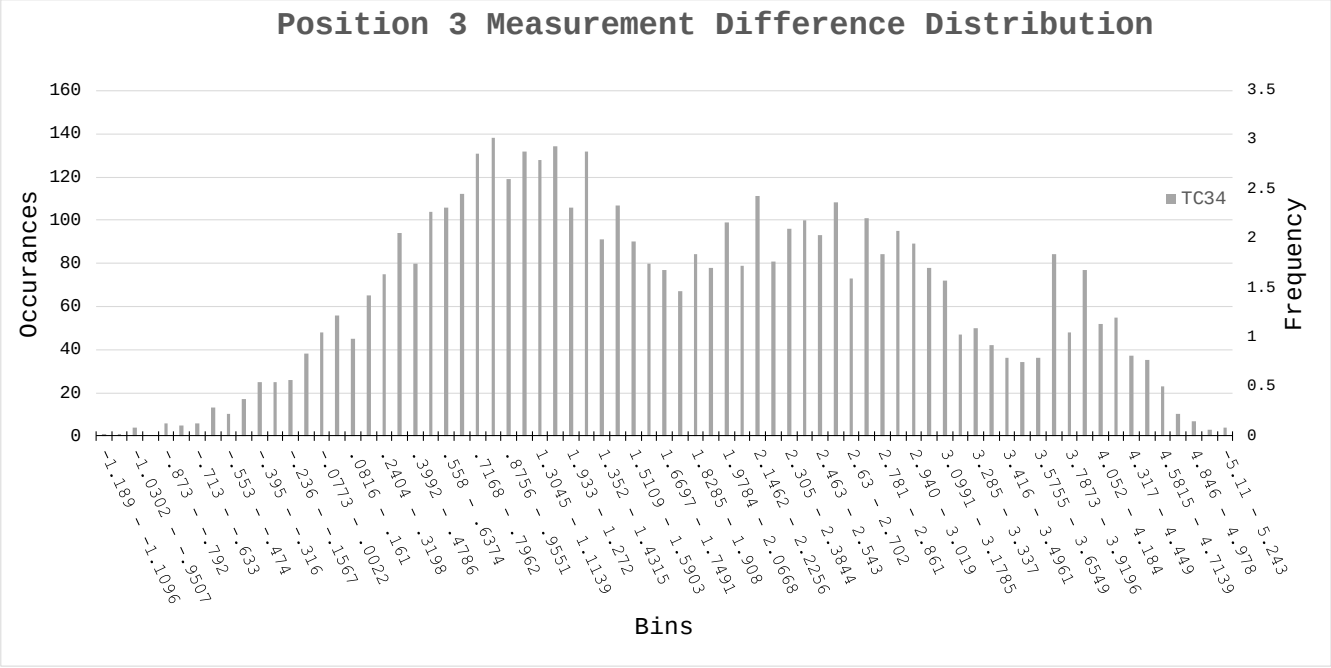

(c)

Figure 16(a-c): Frequency distribution plots for displaying 'R-3' – 'R-4' data for positions 1-3.

Two important details emerge from these figures: first, the data shown in Figure 16(a-b) reflects a bimodal distribution and the data shown in Figure 16(c) reflects a trimodal distribution; however, only Figure 16(a,b) has variances and means separated by a value greater than 2σ [38]. Therefore, only the top and middle position's modes can be analyzed using unimodal, normal, statistics. A square root choice method determines the number of bins in each diagram.

$$k = \sqrt{n} \tag{3}$$

k = number of bins
n = number of data points in data array

$$k\_i = \frac{\max value - \min value}{k} \tag{4}$$

k_i = bin size

The means in each figure, for each mode, are low, with the lowest means corresponding the agreement of MM1 during single-phase heating. The greater means correspond to transition periods during melt. This is an important detail—it implies that the chamber transitions with relatively good thermal symmetry. Another key detail is the agreement between 'R-3' and 'R-4' is high in the top and middle positions with approximately 80% of the entire data set falling with in ± 2.2 ºC.

The bottom position's data is poorer with 60% of the data recorded falling with in ± 2.2 ºC. However, heat conduction and plume formation at the lowest axial location in the chamber is the most unpredictable. Analyzing the BAPs in Figure 19 and the thermal characteristic plots in Figure 9 (c) supports this claim.

When viewing all the plots together it is apparent that the mean, mode and standard deviation change as the temperature probes traverse to lower axial locations. This implies that the evolution of the melt front is potentially influenced by the instrument insertion depth. The plots in Figure 17(a-c) are used to further explore this point.

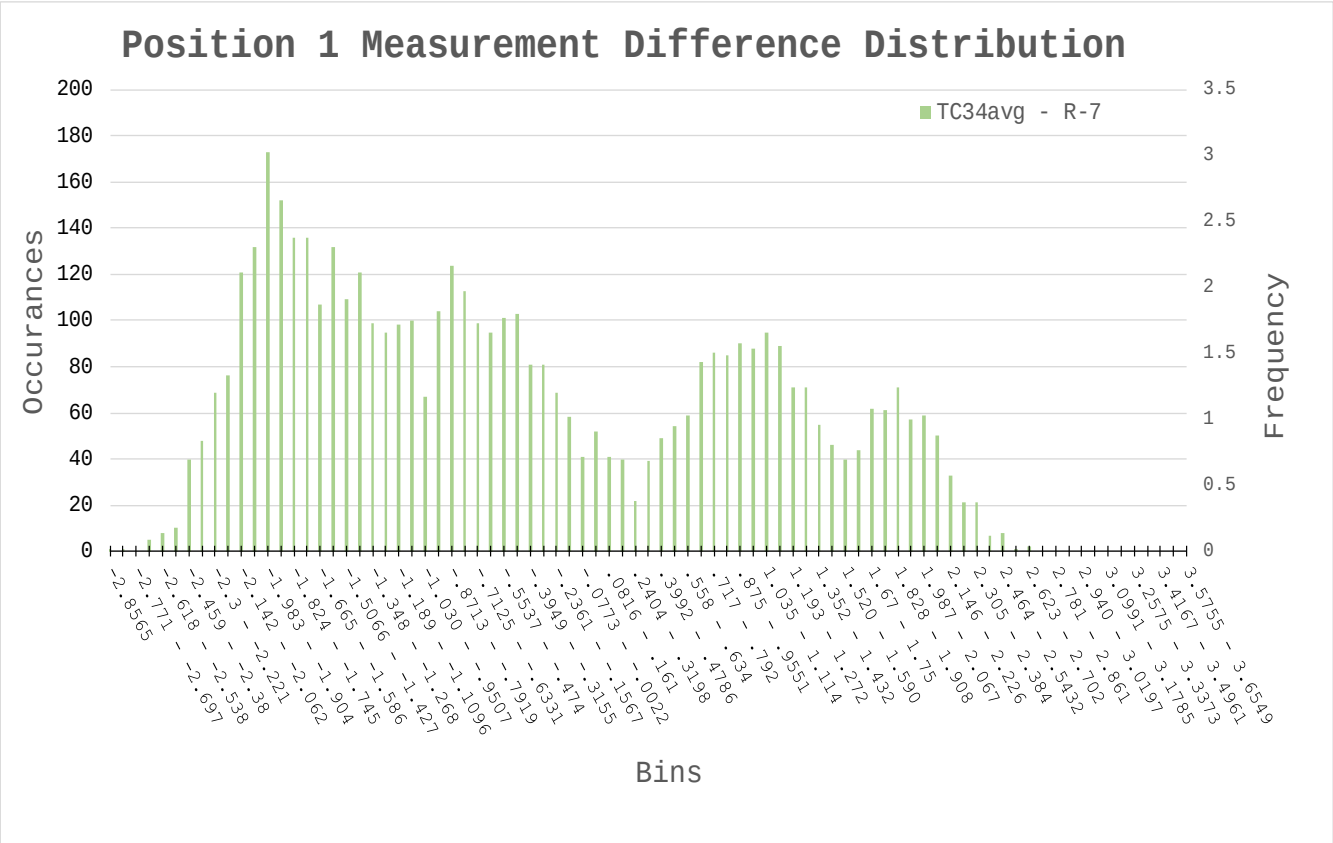

(a)

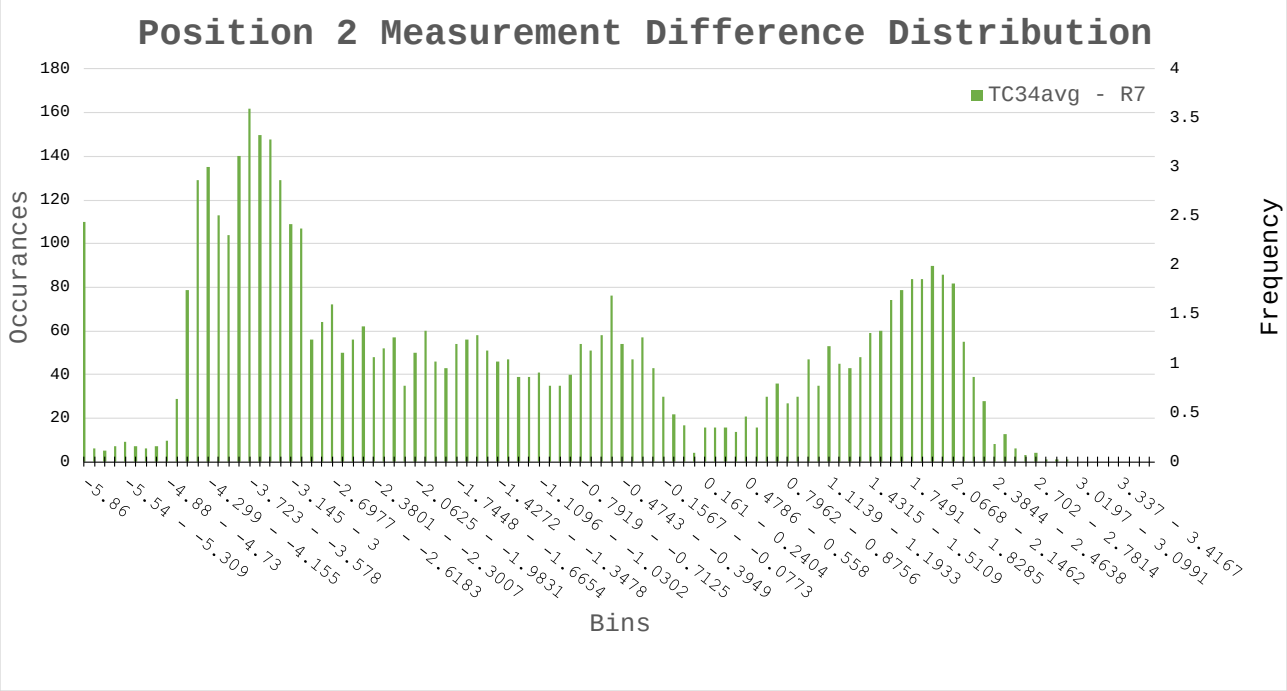

(b)

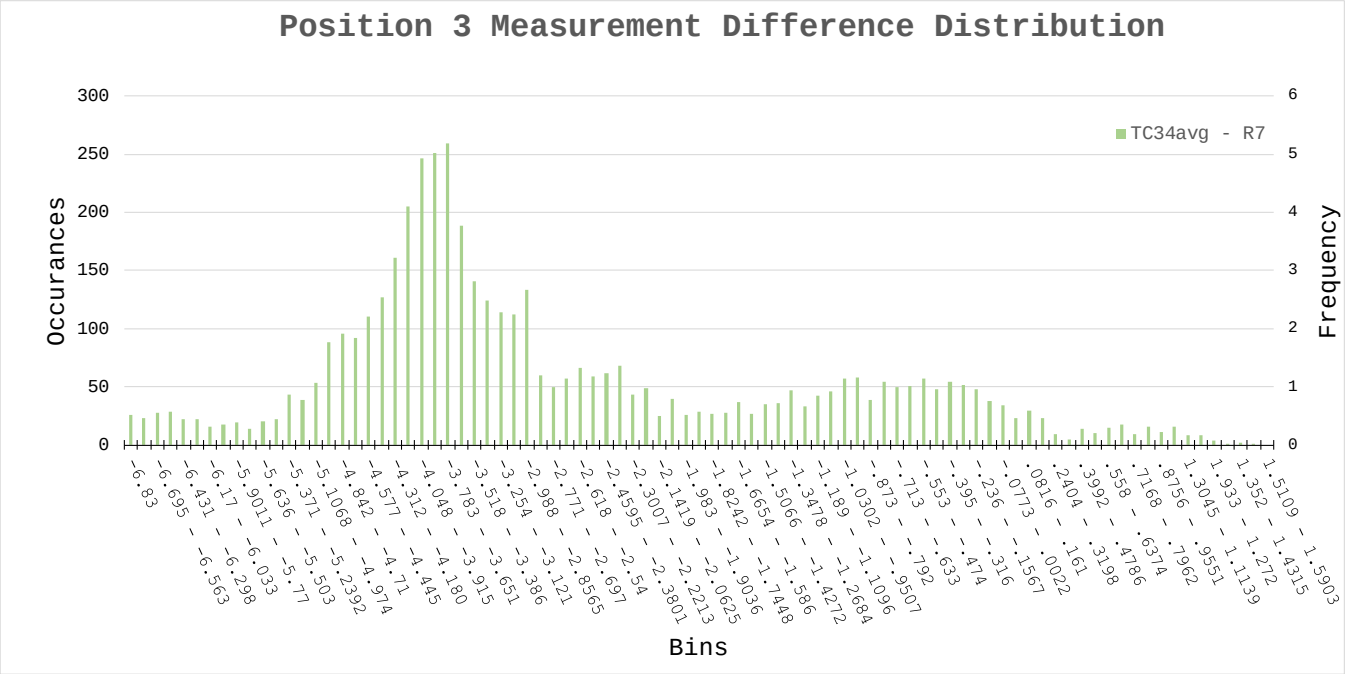

(c)

Figure 18: MM1 vs MM2 frequency distribution.

Shown by Figure 17(a-c), MM1 vs MM2 does not follow any discernable distribution. This implies that the temperature probes do not experience phase change at the same time. The lack of similarity between MM1's TC frequency distribution and MM1's vs MM2's frequency distribution supports the hypothesis that there is an effect due to neighboring thermocouples. The theory gains traction by examining Figure 17(a). At the top position, where the TCs are least inserted into the phase change material, the change in temperature as observed by the probe's tips is nearly equal. The data shows that the disagreement at this location is minimized, suggesting that the physical interplay is reduced. Under the assumption that the disagreement at the top position is purely systematic, then comparing the agreement at the top to the middle and bottom position data set, one would expect all plots should yield the same deviation. However, that is not what is observed. The disagreement grows from the top to the bottom with over 50% of the data falling outside of systematic uncertainty of the instruments. These observations

support the hypothesis that the measurement system does indeed effect the rate of energy transport in a given section. Examination of Figure 19 aids this discussion.

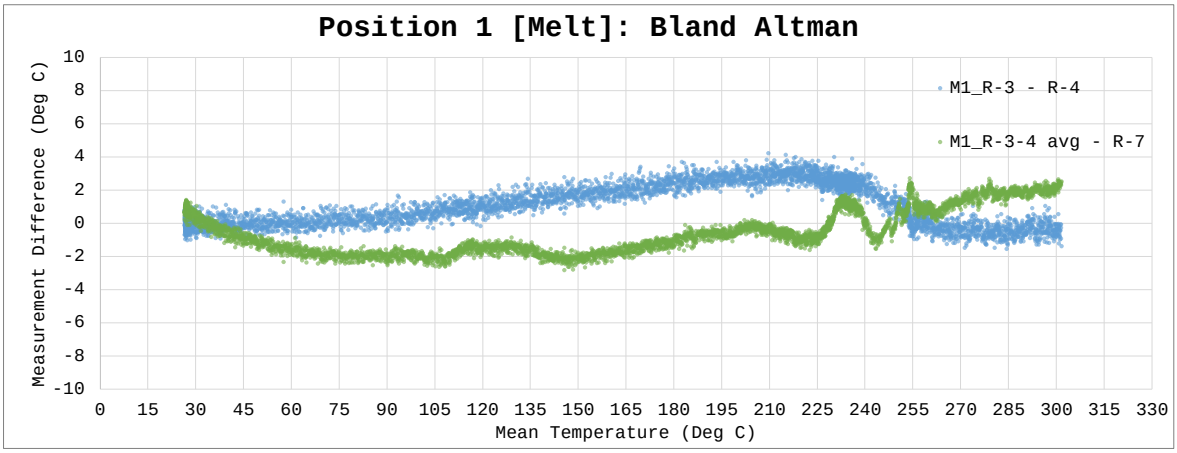

(a)

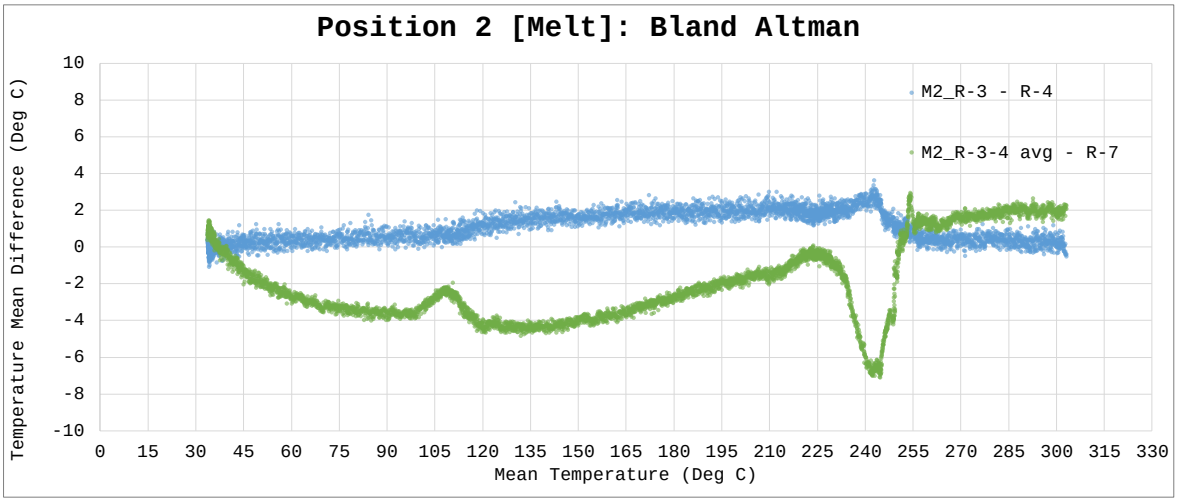

(b)

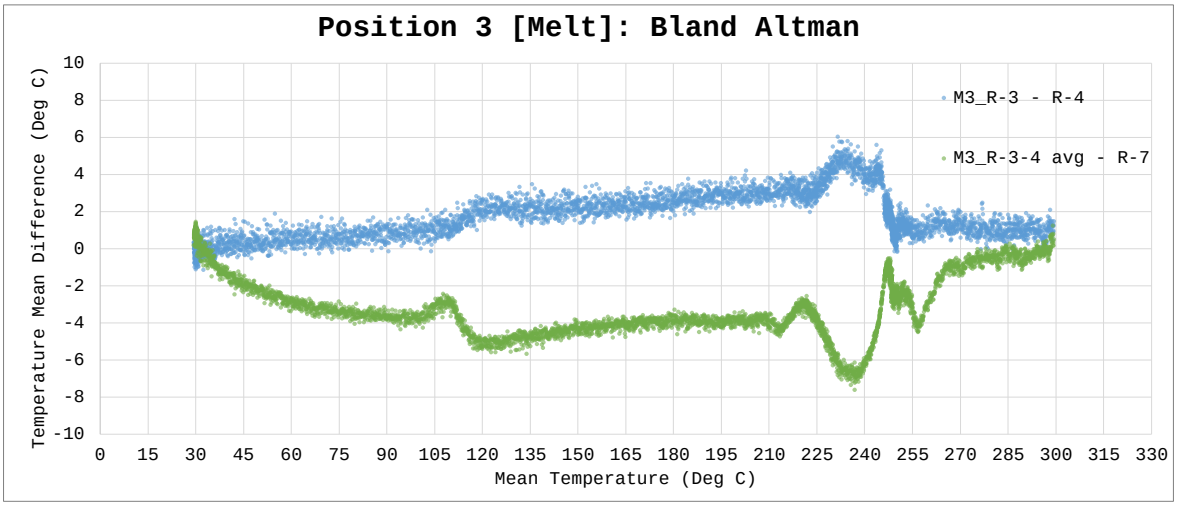

(c)

Figure 19(a-c): Bland Altman plots, bottom to top positions. Each plot displays the temperature difference recorded by the temperature probe agiasnt their mean during the melt phase. MM1 and MM1 vs MM2('R-3' vs 'R-4' (blue) and 'R-3-4 average' vs 'R-7' (green)).

The Bland-Altman plots shown in Figure 19(a-c) reveal two important concepts regarding flow development: first, the enclosure sections containing multiple instruments heat more slowly than the section containing just one instrument. This is shown by analyzing MM2 (comprised of taking 'R3-4 avg' and subtracting it from 'R7' and plotting it against the average temperature between the two methods). The mostly negative data implies that 'R-7' reflects a higher temperature than 'R3-4 avg' and the shape of the plot shows 'R-7' responds more quickly to temperature changes. The data shows at the melt temperature, 'R-7' exhibits a higher temperature implying that this TC registers a liquid state before 'R3-4 avg'. Second, the flow develops symmetrically along the wall in sections containing multiple instruments. The fact that the agreement is significantly higher for MM1 as opposed to MM1 vs MM2 there is evidence that the enclosure experiences good thermal symmetry in sections that contain multiple instruments. To that point, Figure 19 (a) shows agreement is best at the top position indicating that the insertion depth influences the amount of energy being redistributed to the instruments.

After the S-S phase change, the agreement between MM1 and MM2 increases until the TC's register the liquidus temperature, Matter in fact, the measurement method's temperature difference is the most consistent during the conduction dominated phase of the experiment. One reason for this is, during the S-L transition, the MM1 TCs reduce the cross-sectional flow path resulting in a restriction of fluid flow. This naturally leads to the question of how do the TC's influence the results.

Despite flow obstructions, at all positions, the 'R-3' vs 'R-4' plots show high agreement – indicative of symmetric thermal development in their respective sections. Notice MM1 exhibits

an ordered and predictable rising trend that remains close to zero through the duration of heating. This implies that MM1 experiences a near symmetric loading through both conduction and convection dominated phases. That being said, for both MM1 and MM1 vs MM2, quantifying the agreement is challenging; as made clear by Figure 16 and Figure 17, The populations do not follow normal distributions. However, the disagreement shown by MM2 in the Bland-Altman plots and the inconsistent nature of the frequency distribution plots in Figure 17 supports the conclusion that the thermal symmetry in all three sections of the experiment would be improved by the reduction of TCs in the other sections.

4.2.1 Conclusions

In conclusion, the data suggests that sections containing equal amounts of TCs experience symmetric heating; additionally, the further TCs extend into the salts, the more influence they have on the flow pattern. The Bland-Altman and frequency distribution plots illustrate that the agreement between the TCs that comprise MM1 is far greater than the agreement of the TC's that comprise MM1 vs MM2. Moreover, the agreement is highest at the top position.

4.3 Computational Simulations

Studies show improving the rate heat transfer between the LHES material and conduction enhancing mediums significantly improves the efficiency of a LHES device. Given the complexity of the design space, researchers have been tending toward numerical techniques for optimizing the energy transfer in and out of devices. Mike Augspurger, a colleague at the University of Iowa, developed a numerical method for modeling conjunctive heat transfer problems. He adapted his code to match the geometry and boundary conditions of the experimental test set up. He and I partnered to synthesize our findings in order to better understand the flow physics inside in the chamber. A few important simulation details are laid out here, however, for a full account, please refer to Mike's Thesis "Improving the Performance of Finned Latent Heat Thermal Storage Devices Using a Cartesian Grid Solver and Machine-Learning Optimization Techniques".

4.3.1 Simulation Setup

Given the complexity of the experimental domain, adaptations were made to the numerical solver to reduce the computational expense. The simulation domain, seen in Figure 20, was restricted to the volume below the liquid salt level.

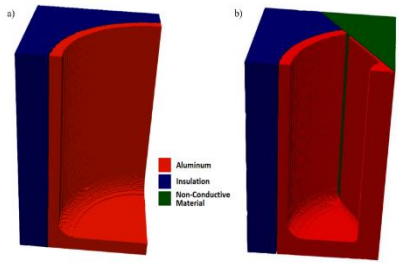

Figure 20: Simulation domain. (a) no fin

This act is predicated on a few assumptions: first, the air above the salts would not impact the flow at the surface and secondly, changes in volume of the salt, due to temperature change, would be negligible, lastly, the specific heat, c_p, would be held constant. Additionally, the cross section of the enclosure was reduced to a slice; so for the no-fin case, the simulation uses one quarter of the experimental domain, while the finned case contains one sixth of the domain. The latter domain reduction makes the assumption that the flow is axially symmetric within the no-fin chamber and is symmetric with in the subdivisions created by the fins in the finned case. In order to reduce the domain, further a wedge of non-conductive material was introduced into the domain, slicing the fin at its midpoint. Given this, the following domain setup shown in Figure 21 was used.

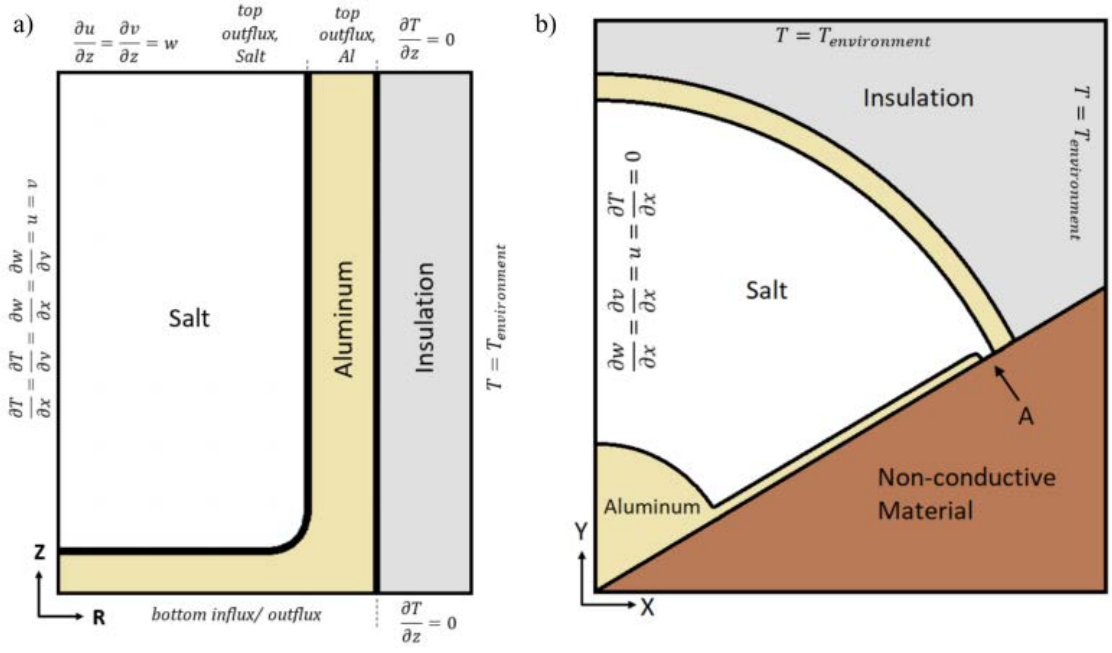

Figure 21: Domain setup and boundary conditions. (a) Axial cross section of the no-fin domain. Because of the rectangular volume, insulation is variable in different radial directions. (b) Radial cross section of the finned domain. "A" marks the point where the effects of a non-physical no-slip condition are assumed negligible.

4.3.2 Material Properties and Boundary Conditions

In both the finned and no-fin cases, a Dirichlet boundary condition was applied to the two external vertical sides using a temperature condition, with the temperature set at the $T_{environmental}$, where $T_{environmental}$ is dependent upon the experimental conditions. The finned case was modeled with both internal vertical sides having symmetric boundaries on the internal vertical side that meets the salt. In a like manner, the finned case has a symmetric boundary on the internal vertical side with the salt. However, the second internal vertical boundary in the finned case is at the interface between the TESD and the non-conductive material. This interface was designed to act as a symmetric boundary condition. The top and bottom boundaries for the insulation have a no flux condition, as axial heat transfer out of the enclosure was assumed negligible. The velocity at the top is symmetric.

Initial estimates of the BCs are made by transiently estimating the average sensible and latent heat in the enclosure, initial estimates regarding heat input are refined through trial-and-error iterations of the simulation. Table 5 shows the simulation details.

Table 5: Simulation details

Geometry	Simulation Type	Length (m)	Initial Condition (°C)	Neumann BCs in Established Simulation (in Total Flux)		Dirichlet BCs (°C)
				Bottom (W) ($T_{ave,\,Al}$ in °C)	*Top (W) (t in min., $T_{ave,\,Al}$ in °C)*	*Insulation*
No-fin	*Charge*	70	22.5	138	27.30 + ((t-20)*0.004)	22.5
	Discharge	500	275	< 100 min: 0.141* ($T_{ave,\,Al}$ -22.5) > 100 min: 0.130* ($T_{ave,\,Al}$ -22.5) *Flux is evenly split between top and bottom*		22.5
Finned	*Charge*	80	30	138	21.95 + ((t-35)*0.0011)$^{1.2}$	30
	Discharge	500	275	< 100 min: 0.131* ($T_{ave,\,Al}$ -30) > 100 min: 0.112* ($T_{ave,\,Al}$ -30) *Flux is evenly split between top and bottom*		30

The boundary conditions for the top and bottom vary with the average temperature with in the aluminum for discharging simulations but vary with time for the charging simulations. The charging simulations were defined by fitting the simulation TC curves to the experimental TC curves through trial-and-error using a dynamic flux that is a function of time.

4.3.3 Results

Four simulations were run in order to replicate charging and discharging for the experimental fin and no-fin cases. Although the simulations as a whole seem to replicate the experimental data very well there are a few notable differences. In the fin simulations center TC registers a higher temperature throughout the trial than the experiments. The reasons for this are presumed to be due to the fact that the center TC did have perfect contact with the inside wall of the aluminum (a necessary design feature for the safe traversing of the instrument), or that the simulations did not account for the stainless steel super heli-coil or the stainless steel set screw at the fin's base. Another discernable difference is the capturing of plume formations. Given the simulations modeled a fraction of the domain, there are some small and expected dissimilarities present between the experimental and computational results regarding the time and location of plume formation. However, given necessary assumptions made for both the numerical solver and the experiments, the general melt pattern was found to be well very captured by the simulations. The following figures (Figure 22 - Figure 25) show qualitatively how similar the simulations are to the experimental data.

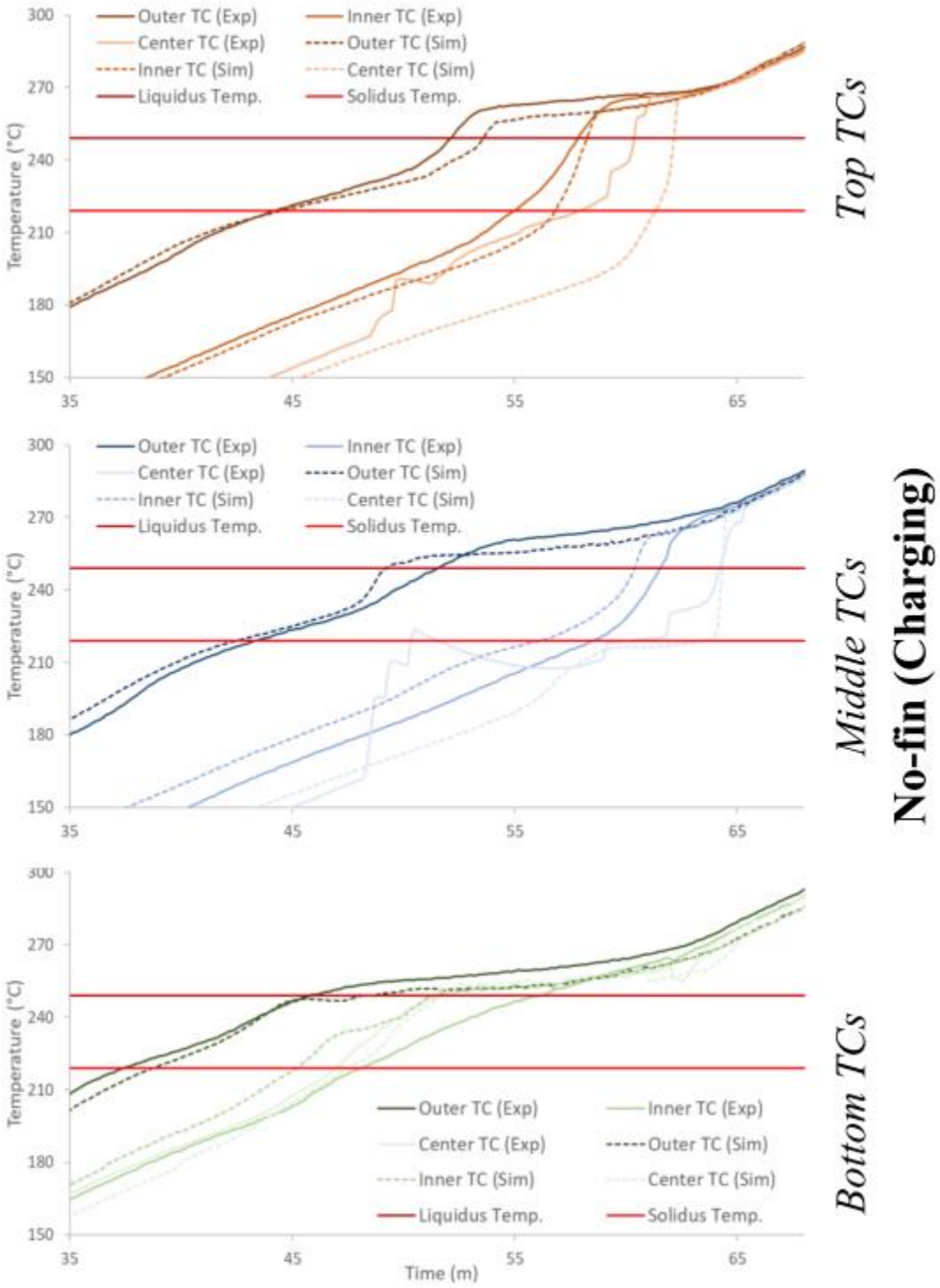

Figure 22: No fin charging thermal characteristics for the top middle and bottom TCs

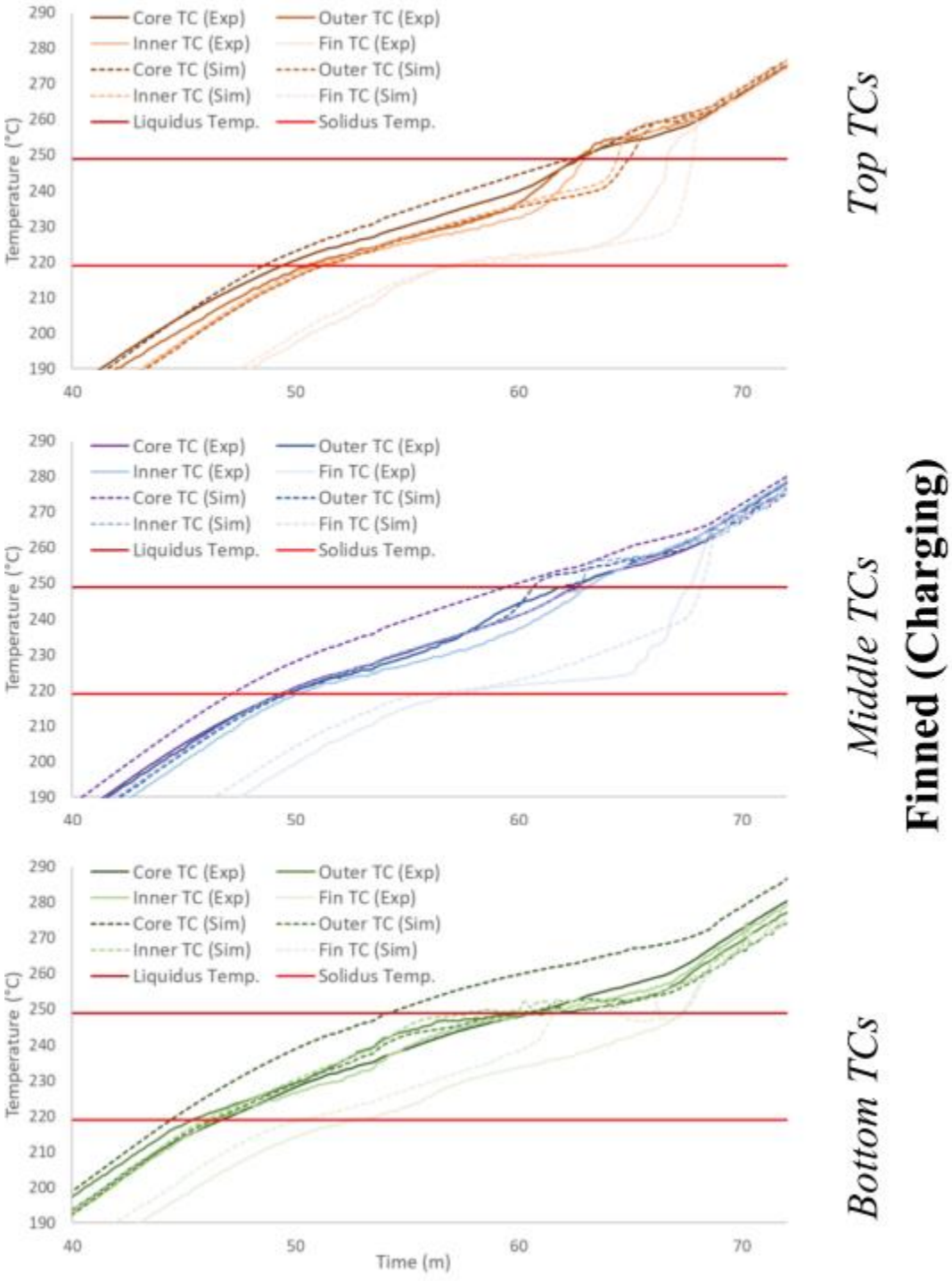

Figure 23: Finned thermal characteristics for the top middle and bottom TCs

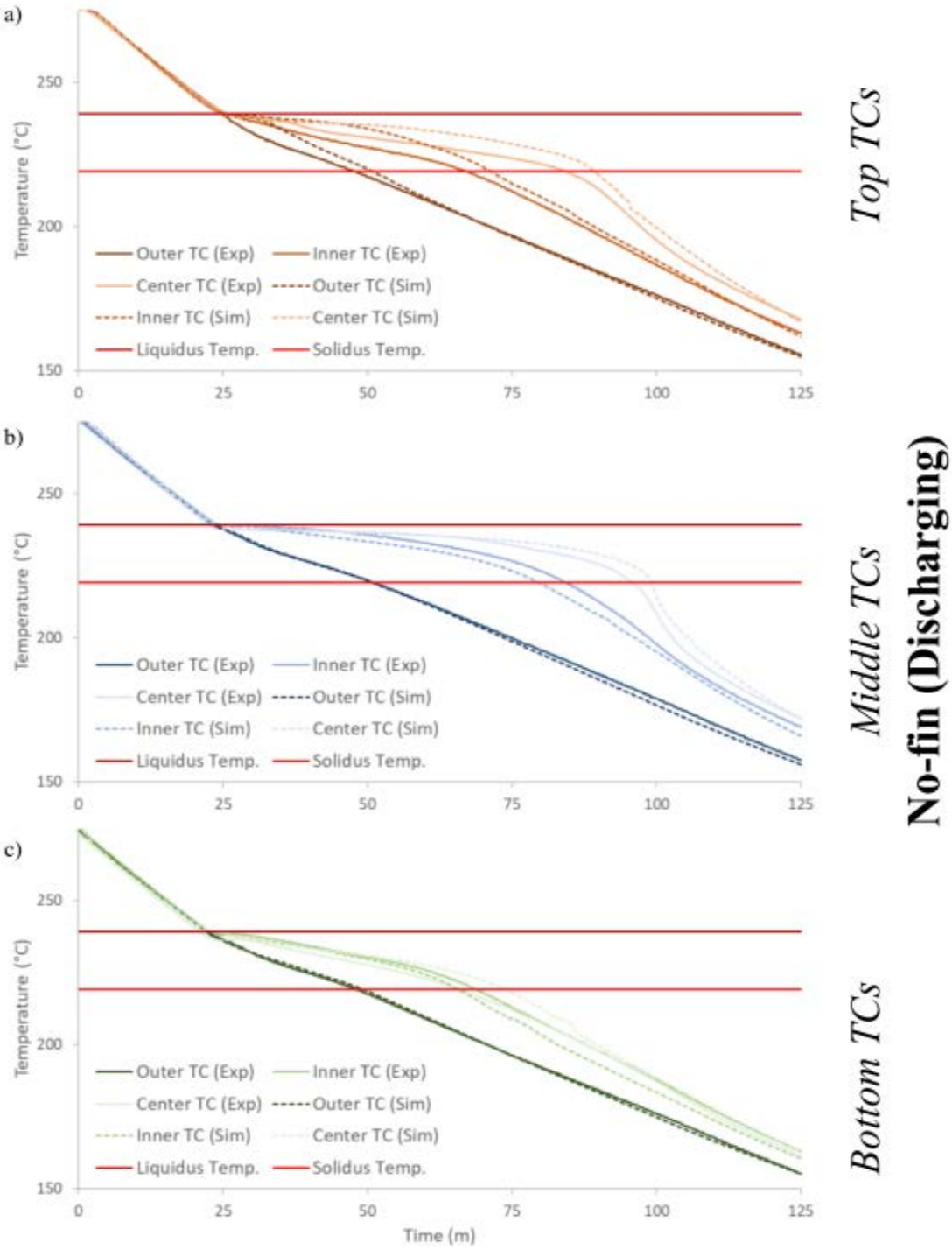

Figure 24: Solidification plots for the top middle and bottom TCs for the No-Fin case

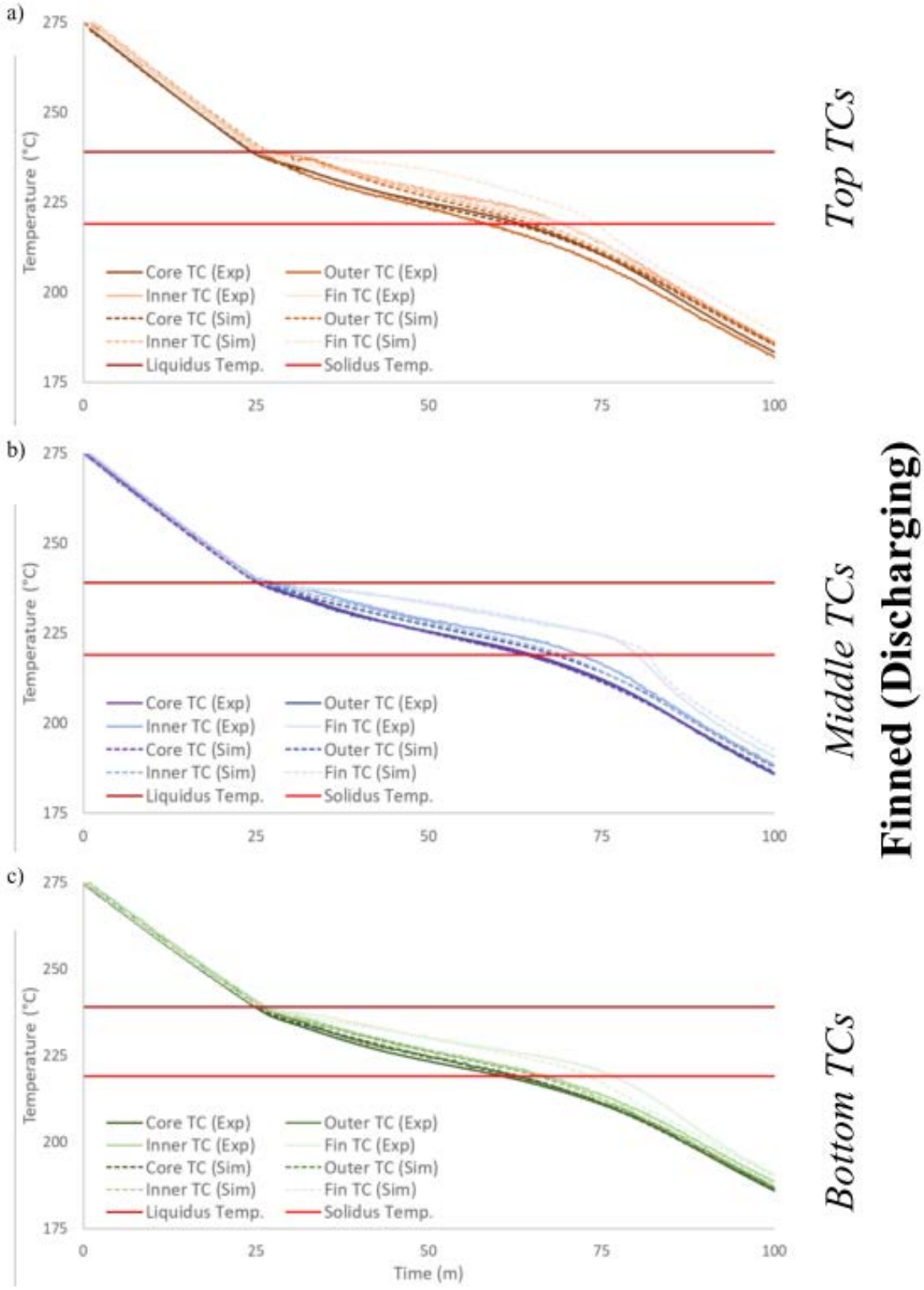

Figure 25:Finned discharging for top, middle and bottom positions.

Notice that the agreement is greater during solidification than melting. Furthermore, that the temperatures agree highly through all stages. The advantage of numerical simulations lies in the figures below. The inflection points in the thermal characteristic that were captured experimentally can be shown using 3-D simulations. As a result, Mike was first to identify four distinct phases of melt. The development of these phases are influenced by the geometry of the two cases.

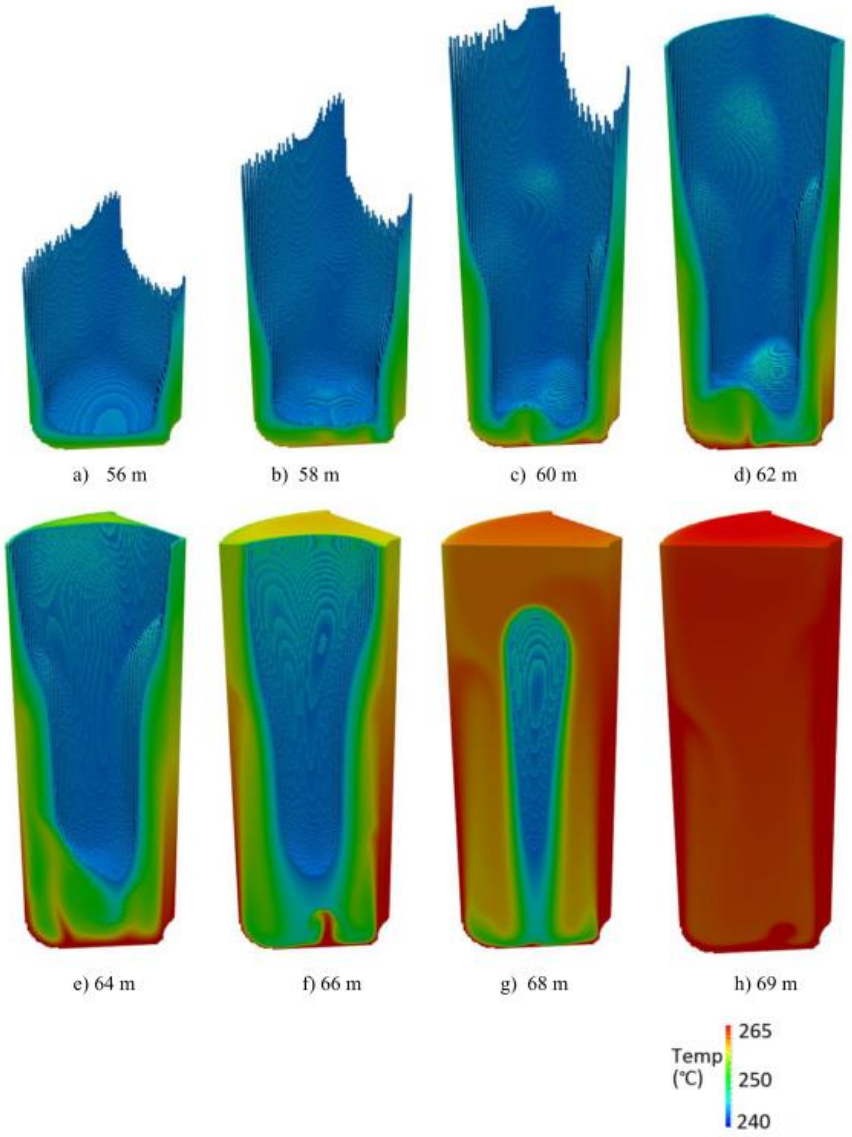

Figure 26: Development of the melt in the finned chamber from 56 - 69 minutes. The solid portion shown in the image shown is the liquid portion of the salts 80% to 100% liquid fraction. The non-visible portion in the center is the solid mass.

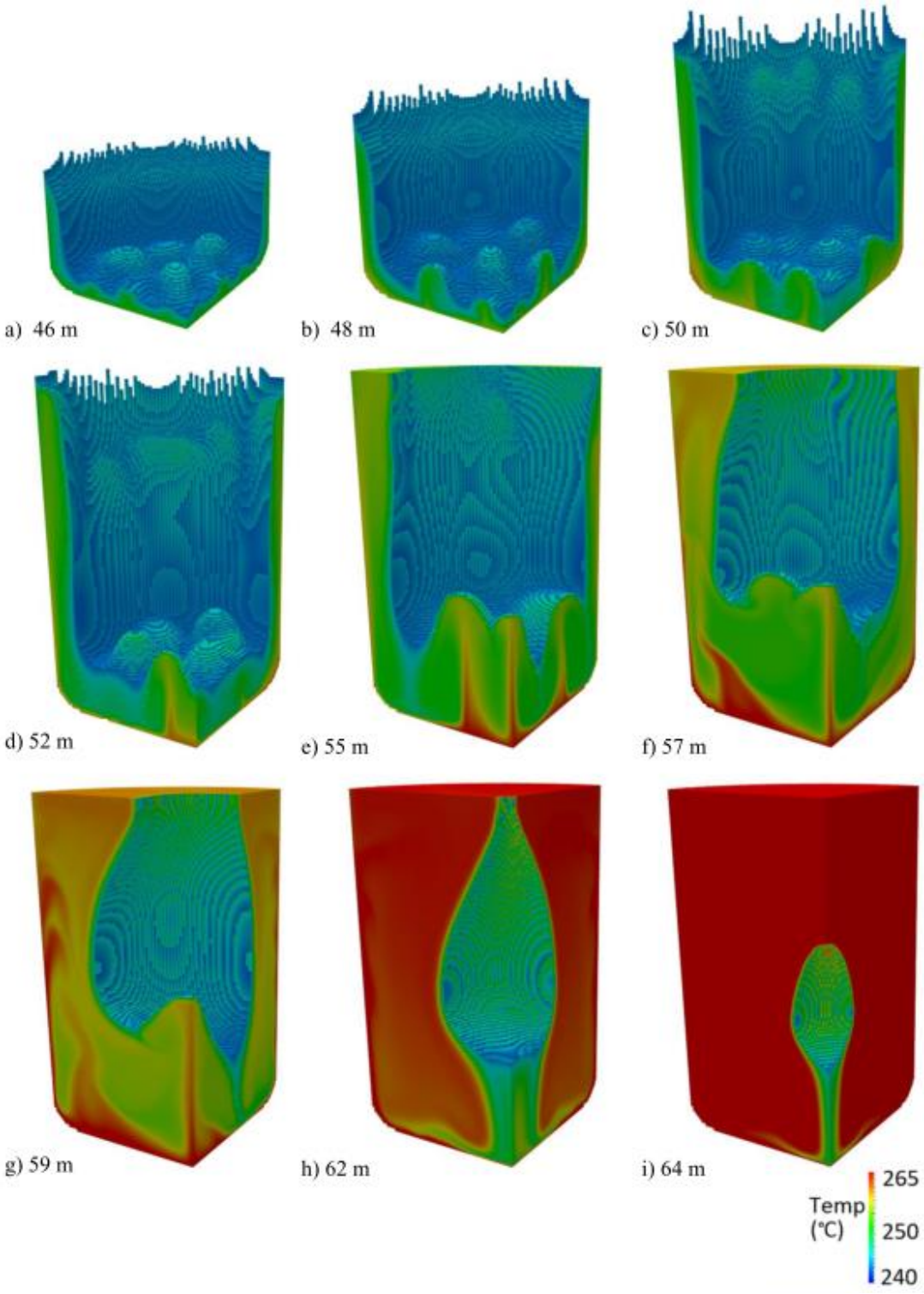

Figure 27: no-fin heating phase shown from 25 - 65 minutes. The floating image in the center of the enclosure represents the solid portion of the salts (0.8<Fls<1.0). Surrounding the aluminum container is the melted portion.

The first phase of melting noticed through the simulations was “thin layer melting”. This is a region where convective heating is minimal and restricted by the surrounding salt. This stage lasts longer in the finned case as opposed to the no-fin case. The major take away here being that the higher mass of aluminum in the finned case more effectively spreads heat to the salt this is evident by the time it takes for plumes to develop inside this geometry. Additionally, the simulations show that there is a greater surface area that experiences ‘thin layer melting’ in the fin case as opposed to the no fin cases.

The second phase of melting is “bottom dominated melting”. In this stage, the formation of plumes begins dominating the convective cell growth. These cells are important to the spreading of heat throughout the chamber. 9 plumes can be seen forming in the no-fin enclosure before merging into one plume. In the finned case, due to the narrowness of the sections, the formations of plumes is greatly inhibited.

The third phase of melting is “side dominated melting”. Here, the convective flows developed during bottom dominated melting gain strength and begin to move up the sides of the chamber. This type of heating develops quickly in the finned case due to the amount of vertical conduction enhancement. The no-fin case the bottom and side convective cells grow simultaneously. This results in a slower convective cell growth development relative to the finned case.

The last phase of melting is “top dominated melting”. The simulations show that the core of unmelted salts at the center of the enclosure, or in the center of a finned section, are further melted from the top down, despite heat being supplied to the bottom of the enclosure. The

simulations show that once the side dominated stage matures, the melt boundary begins to move down into the remaining unmelted core. The simulations reveal that the last remaining salts after the side dominated melting stage has matured exists about one-third of the way up from the bottom of the enclosure.

The melt development characteristics Mike identifies are supported by the melt characteristics found in the experimental data. 'Thin layer melting" is readily observed by the 'r_f', 'R' and 'center' TCs; each TC reaches the eutectic and liquidus temperatures before 'r', and they also do so from bottom to top. The same is true in the no-fine case, 'R' reaches the eutectic and liquid temperature sooner at each position. This indicates that the salts in contact with the aluminum are the first to liquefy.

"Bottom dominated melting" is also readily apparent. For example, in the no-fin case; Figure 12 (c) shows that 'center's' heat rate climbs faster than 'r' after the salt mass reaches the eutectic temperature. This is indicative of early plume formation. Moreover, in Figure 12 (b), 'center' reaches the eutectic temperature ~10 minutes sooner than 'r'. Both which provide evidence that the no-fin case experiences rapid convective cell growth and plume development at the bottom of the enclosure. "Bottom dominated heating" in the fin case is not as easily identifiable, however, the experimental data shows that the bottom most position reaches a fully liquid state well before the top or middle.

The experiments provide good evidence of "side dominated melting". Both the fin and no-fin thermal characteristics show that 'R' melts far sooner than 'r' or 'center'. As the salts at the

bottom of the enclosure melt ~3 minutes sooner than the salts at the top, significant melting along the length of the enclosure has occurred. The fin case's data also reveals that significant melting has occurred along the length of the chamber by the time the top TC's register the medium reaching the eutectic temperature.

Lastly, Table 3 shows that the top of the salts begin melting before the salts at the center do. When the salts at the top of the enclosure have melted, the rate of heat transfer at the center of the enclosure increases as shown in Figure 12 (b). This implies that the convective flow patterns have developed along all the sides of the solid mass.

Salt solidification is less complex than melting. Mike's simulations find that the maximum velocity magnitudes during phase change are an order of magnitude lower than those found in the charging simulations; as a result, conduction becomes the dominating mode of heat transfer. Figure 28 and Figure 29 depict the boundary developing in similar ways for both cases. This results in a majority of the heat leaving through the bottom and top surfaces of the enclosure. This is as expected given the lack of insulation in those areas. These figures show the importance of optimizing the conduction enhancement for effective heat transfer during discharge. As the salts accumulate on the aluminum surface the rate will decline.

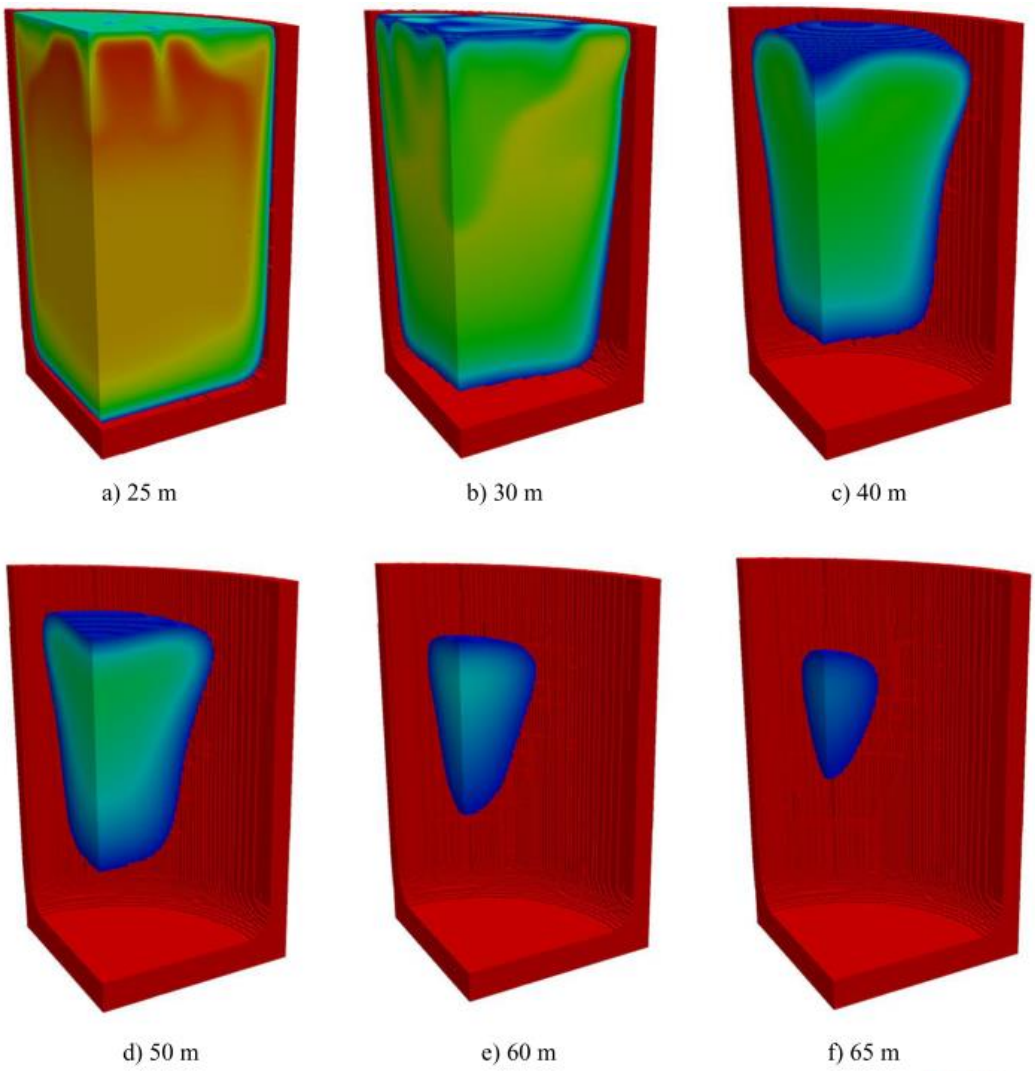

Figure 28: no-fin solidification phase shown from 25 - 65 minutes. The floating image in the center of the enclosure represents the liquid portion of the salts (0.8<Fls<1.0) surrounding the aluminum container (in red).

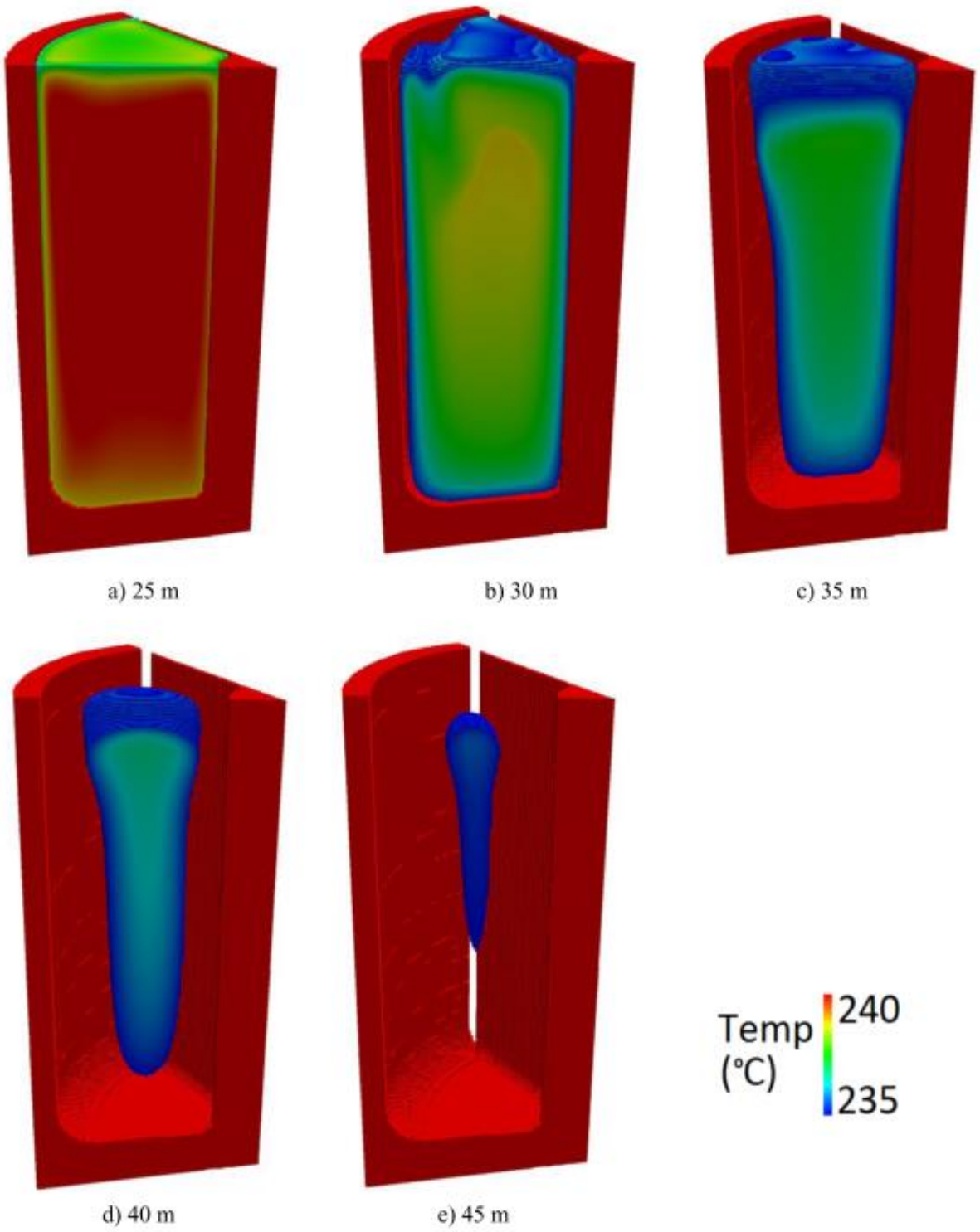

Figure 29: Finned test case solidification from 25 - 28 minutes. The floating image at the center of the enlcosure represents the liquid portion, yet to solidify (0.8<Fls<1.0). The asluminum enclosure and core are depricited in red.

4.3.4 Conclusions

The simulation temperature probe data shows agreement with the experiments as demonstrated by Figure 22 - Figure 25. Furthermore, the development of the melt front shown in simulation figures 28 and 29 agree well with what is observed experimentally. The important take away from this combined work is the finned design leads to more effective melting and solidification relative to the no-fin design. Despite the difficulty in directly comparing the two tests cases to each other, the time taken for a fully liquid medium to exist after the onset of melt, within the enclosure happens sooner in the finned case relative to the no-fin case. The reason for this is governed by the influence of the vertical flat plats on early convective transport, additionally; the finned design moves more quickly through the bottom-dominated heating phase than the no-fin design.

Chapter V – Conclusions

This work is designed to contribute to global sustainability measures by investigating latent heat energy storage (LHES) cooking technology. A conduction enhancement method is investigated by recording the temperatures distribution at discrete radial and circumferential locations in an aluminum enclosure containing 650 grams of solar salt. The conduction enhancement and no conduction enhancement methods are explored by analyzing the temperature data and making comparisons between the test cases. Using these data, investigating the effect of conduction enhancement on system performance, the effect of the measurement system on measurement accuracy and the efficacy of a computational simulation are possible.

The results from this work show first, how melting occurs within the enclosure and second, the results of using conduction enhancement to increase thermal transport in an unconducive media. The test cases show that the first regions to experience melt are the bottom and walls in the enclosure, with the top and center of the salts following. Where the two test cases are distinguished is in time taken for convection cells to span the length of the solid salt media. In the fin case the data shows that heat is distributed more effectively due to the vertical fin arrangement and is imperative to development of convection cells that span the length of the salt/aluminum interfaces early on in the experiment. As a result of increased heat spreading, the top of the enclosure melts 4 minutes sooner than the salts at the center relative to the no-fin case. Furthermore, the fin test case's data showed that the it achieved a full liquid state sooner after the onset of melt when compared with the no fin case. This suggest that the same method of conduction enhancement at a greater scale would significantly reduce the melt time.

Additionally, comparing the plots of the differences between the two measurement methods against their mean showed an effect of measurement system on system performance. The Bland Altman plots, in conjunction with the frequency distribution diagrams, revealed that the second measurement method, relative to the first, does express an influence on the heat transfer physics taking place in the enclosure. This is an important finding as it suggests that future experiments will have to consider the characteristic length of the instruments future experiments.

Lastly, computational results reveal show that vertical conduction enhancement decreases the time taken for the solution to move from bottom-dominated heating to side dominated heating. These results suggest that in designing a LHES device the primary focus should be finding means to encourage strong vertical circulation patterns.

Chapter VI – Future Work

Experimentally investigating the phase change material that comprises a solar cooker is an essential step to developing a viable prototype. Synthesizing the results from this work with new experimental plans that test alternate conduction enhancement methods coupled with parsimonious instrumentation are some of the most natural next steps. Future developments for this project would look to utilize optimal conduction enhancement methods used to charge and discharge the latent heat. After establishing an experimental procedure for conduction enhancement, charging and discharging, exploring different forms of insulation would come next. Lastly, using the data collected in this project, it would be useful to create a geometry optimized cooker with an experimental lab setup that matched diurnal cycles. Once this was fully developed creating full-scale experiments from this data and experimenting on the effectiveness would be the natural next step.

Lastly, a greater understanding could be found in the relationship of measurement devices on the development of flow patterns. This idea could be used to encompass other important areas of experimentation such as heat input, insulation and discharge.

Works Cited

1. Watson J, Sauter R. Sustainable innovation through leapfrogging: a review of the evidence. *Int J Technol Glob*. 2011;5(3/4):170–189. doi:10.1504/IJTG.2011.039763

2. Smith KR, Mehta S, Maeusezahl-Feuz M. Indoor air pollution from household use of solid fuels. *Comp Quantif Heal risks Glob Reg Burd Dis Attrib to Sel major risk factors*. 2004:1435-1493. doi:10.1078/1438-4639-00224

3. Rehfuess E. Fuel for life: household energy and health. *Geneva World Heal Organ*. 2006:1-23. doi:http://www.who.int/indoorair/publications/fuelforlife/en/

4. Granich R, Gupta S, Hersh B, et al. Trends in AIDS deaths, new infections and ART coverage in the top 30 countries with the highest AIDS mortality burden; 1990-2013. *PLoS One*. 2015;10(7):1-16. doi:10.1371/journal.pone.0131353

5. Murray CJL, Rosenfeld LC, Lim SS, et al. Global malaria mortality between 1980 and 2010: A systematic analysis. *Lancet*. 2012;379(9814):413-431. doi:10.1016/S0140-6736(12)60034-8

6. World Health Organization. Burden of disease from Household Air Pollution for 2012. 2014;35(February):17. doi:10.1016/S0140-6736(12)61766-8.Smith

7. World Health Organization. WHO Expert Meeting: Methods and tools for assessing the health risks of air pollution at local, national and international level. Meeting report. 2014;(May):1-112. http://www.euro.who.int/__data/assets/pdf_file/0010/263629/WHO-Expert-Meeting-Methods-and-tools-for-assessing-the-health-risks-of-air-pollution-at-local,-national-and-international-level.pdf.

8. Bruce N, Rehfuess E, Mehta S, Hutton G, Smith K, Asia S. Indoor Air Pollution. *Dis Control Priorities Dev Ctries*. 2002:793-817.

9. Zhang J, Smith KR. Indoor air pollution: A global health concern. *Br Med Bull*. 2003;68(November):209-225. doi:10.1093/bmb/ldg029

10. Hutton G, Rehfuess E, Tediosi F, Weiss S. Evaluation of the costs and benefits of household energy and health intervantions at global and regional levels. 2006:19. http://www.who.int/indoorair/publications/summary_household_energy_health_intervention.pdf.

11. Hutton G, Rehfuess E, Tediosi F. Evaluation of the costs and benefits of interventions to reduce indoor air pollution. *Energy Sustain Dev*. 2007;11(4):34-43. doi:10.1016/S0973-0826(08)60408-1

12. Bailis R, Drigo R, Ghilardi A, Masera O. The carbon footprint of traditional woodfuels. *Nat Clim Chang*. 2015;5(3):266-272. doi:10.1038/nclimate2491

13. Masera OR, Bailis R, Drigo R, Ghilardi A, Ruiz-Mercado I. Environmental Burden of Traditional Bioenergy Use. *Annu Rev Environ Resour*. 2015;40:15.15.301. doi:10.1146/annurev-environ-102014-021318

14. IEA. Energy and poverty. 2002:365-393. http://www.worldenergyoutlook.org/media/weowebsite/2008-1994/weo2002_part2.pdf.

15. IPCC. *Climate Change 2014: Mitigation of Climate Change*.; 2014. doi:10.1017/CBO9781107415416

16. Perkins R. Environmental leapfrogging in developing countries : A critical assessment and reconstruction. 2003;27:177-188.

17. Urban F. *Sustainable Energy for Developing Countries: Modelling Transitions to Renewable and Clean Energy in Rapidly Developing Countries*.; 2009. doi:10.1088/1755-1307/6/9/192020

18. IPCC. *Climate Change 2014: Synthesis Report. Contribution of Working Groups I, II and III to the Fifth Assessment Report of the Intergovernmental Panel on Climate Change*.; 2014. doi:10.1017/CBO9781107415324.004

19. Jegadheeswaran S, Pohekar SD. Performance enhancement in latent heat thermal storage system: A review. *Renew Sustain Energy Rev*. 2009;13(9):2225-2244. doi:10.1016/j.rser.2009.06.024

20. Velraj R, Seeniraj RV, Hafner B, Faber C, Schwarzer K. Heat Transfer Enhancement in a Latent Heat Storage System. *Sol Energy*. 1999;65(3):171-180. doi:10.1016/S0038-092X(98)00128-5

21. Walter H, Beck A, Hameter M. Influence of the Fin Design on the Melting and Solidification Process of NaNO 3 in a Thermal Energy Storage System. *J Energy Power Eng*. 2015;9:913-928. doi:10.17265/1934-8975/2015.11.001

22. Bauer T, Tamme R, Christ M, Öttinger O. PCM-Graphite Composites for High Temperature Thermal Energy Storage. *ECOSTOCK, 10th Int Conf Therm Energy Storage*. 2006:19.

23. Fan L, Khodadadi JM. Thermal conductivity enhancement of phase change materials for thermal energy storage: A review. *Renew Sustain Energy Rev*. 2011;15(1):24-46. doi:10.1016/j.rser.2010.08.007

24. Walter H, Beck A, Hameter M. Transient Analysis of an Improved Finned Tube Heat Exchanger for. 2016:1-14.

25. Vogel J, Felbinger J, Johnson M. Natural convection in high temperature flat plate latent heat thermal energy storage systems. 2016;184:184-196. doi:10.1016/j.apenergy.2016.10.001

26. Okello D, Nydal OJ, Banda EJK. Experimental investigation of thermal de-stratification in rock bed TES systems for high temperature applications. *Energy Convers Manag*. 2014;86:125-131. doi:10.1016/j.enconman.2014.05.005

27. Telkes M. Solar cooking ovens. *Sol Energy*. 1959;3(1):1-11. doi:http://dx.doi.org/10.1016/0038-092X(59)90053-2

28. Lane GA. *Solar Heat Storage: Latent Heat Material Volume I*. CRC Press; 1983.

29. Telkes M. Space Heating with Solar Energy Author (s): Maria Telkes Source : The Scientific Monthly , Vol . 69 , No . 6 (Dec ., 1949), pp . 394-397 Published by : American Association for the Advancement of Science Stable URL : http://www.jstor.org/stable/19584. 1949;69(6):394-397.

30. Bauer T, Laing D, Tamme R. Overview of PCMs for Concentrated Solar Power in the Temperature Range 200 to 350°C. *Adv Sci Technol*. 2010;74:272-277. doi:10.4028

31. Bauer T, Breidenbach N, Eck M. Overview of Molten Salt Storage Systems and Material Development for Solar Thermal Power Plants. *Wref*. 2012:1-8. doi:234

32. Zalba B, Marín JM, Cabeza LF, Mehling H. *Review on Thermal Energy Storage with Phase Change: Materials, Heat Transfer Analysis and Applications*. Vol 23.; 2003. doi:10.1016/S1359-4311(02)00192-8

33. Rathod MK, Banerjee J. Thermal stability of phase change materials used in latent heat energy storage systems: A review. *Renew Sustain Energy Rev*. 2013;18:246-258. doi:10.1016/j.rser.2012.10.022

34. Sharma A, Tyagi V V., Chen CR, Buddhi D. Review on thermal energy storage with phase change materials and applications. *Renew Sustain Energy Rev*. 2009;13(2):318-345. doi:10.1016/j.rser.2007.10.005

35. Augspurger M, Udaykumar HS. Transient multi-day simulations of thermal storage and heat extraction for a finned solar thermal storage device. *Sol Energy*. 2017;151:48-60. doi:10.1016/j.solener.2017.05.002

36. Ibrahim ElSaeedy H. Thermal Properties of (Na_{0.6}K_{0.4})NO₃ Thermal Storage System in the Solid-Solid Phase. *Int J Energy Power Eng*. 2016;5(2):34. doi:10.11648/j.ijepe.20160502.12

37. Bland JM, Altman DG. Statistical Methods for Assessing Agreement Between Two Methods of Clinical Measurement. *Lancet*. 1986;327:307-310. doi:10.1016/S0140-6736(86)90837-8

38. Holzmann H, Vollmer S. A likelihood ratio test for bimodality in two-component mixtures with application to regional income distribution in the EU. *AStA Adv Stat Anal*. 2008;92(1):57-69. doi:10.1007/s10182-008-0057-2

39. Omega. Thermocouple Tolerance Values, available at <http://www.omega.com/techref/colorcodes.html>. *Thermocouple Toler Values, available <http//www.omega.com/techref/colorcodes.html>*.:1-7. http://www.omega.com/techref/colorcodes.html.